

Eicosanoid signalling blockade protects middle-aged mice from severe COVID-19

<https://doi.org/10.1038/s41586-022-04630-3>

Received: 17 April 2021

Accepted: 11 March 2022

Published online: 21 March 2022

 Check for updates

Lok-Yin Roy Wong^{1,10}, Jian Zheng^{1,10}, Kevin Wilhelmsen², Kun Li³, Miguel E. Ortiz³, Nicholas J. Schnicker⁴, Andrew Thurman⁵, Alejandro A. Pezzulo⁵, Peter J. Szachowicz⁵, Pengfei Li¹, Ruangang Pan¹, Klaus Klumpp², Fred Aswad², Justin Rebo², Shuh Narumiya⁶, Makoto Murakami⁷, Sonia Zuniga⁸, Isabel Sola⁸, Luis Enjuanes⁸, David K. Meyerholz⁹, Kristen Fortney², Paul B. McCray Jr.^{1,3}✉ & Stanley Perlman^{1,3}✉

Coronavirus disease 2019 (COVID-19) is especially severe in aged populations¹. Vaccines against severe acute respiratory syndrome coronavirus 2 (SARS-CoV-2) are highly effective, but vaccine efficacy is partly compromised by the emergence of SARS-CoV-2 variants with enhanced transmissibility². The emergence of these variants emphasizes the need for further development of anti-SARS-CoV-2 therapies, especially for aged populations. Here we describe the isolation of highly virulent mouse-adapted viruses and use them to test a new therapeutic drug in infected aged animals. Many of the alterations observed in SARS-CoV-2 during mouse adaptation (positions 417, 484, 493, 498 and 501 of the spike protein) also arise in humans in variants of concern². Their appearance during mouse adaptation indicates that immune pressure is not required for selection. For murine SARS, for which severity is also age dependent, elevated levels of an eicosanoid (prostaglandin D₂ (PGD₂)) and a phospholipase (phospholipase A2 group 2D (PLA₂G2D)) contributed to poor outcomes in aged mice^{3,4}. mRNA expression of PLA₂G2D and prostaglandin D₂ receptor (PTGDR), and production of PGD₂ also increase with ageing and after SARS-CoV-2 infection in dendritic cells derived from human peripheral blood mononuclear cells. Using our mouse-adapted SARS-CoV-2, we show that middle-aged mice lacking expression of PTGDR or PLA₂G2D are protected from severe disease. Furthermore, treatment with a PTGDR antagonist, asapiprant, protected aged mice from lethal infection. PTGDR antagonism is one of the first interventions in SARS-CoV-2-infected animals that specifically protects aged animals, suggesting that the PLA₂G2D–PGD₂/PTGDR pathway is a useful target for therapeutic interventions.

Mice are naturally resistant to infection with SARS-CoV-2, as a result of incompatibility between the viral surface spike (S) glycoprotein and mouse angiotensin-converting enzyme 2 (mACE2)⁵. To enable murine infection with SARS-CoV-2, human ACE2 (hACE2) has been provided by genetic manipulation of the mouse genome or exogenously using viral vectors. Transgenic expression of hACE2 (refs. ^{6–9}), complete or partial replacement of mACE2 with hACE2 (hACE2 knock-in)¹⁰ or administration of viral vectors expressing hACE2 all sensitize mice for infection^{11,12}. Alternatively, the S protein of SARS-CoV-2 has been altered using reverse genetics to enable binding to mACE2 (refs. ^{13,14}). SARS-CoV-2 has been adapted to mice by targeting amino acids at positions 498 and 499 (Q498Y/P499T) or 501 (N501Y). The resulting viruses can infect mice, although the resulting infection is very mild. However, further virus passage through mouse lungs results in increased virulence¹⁵. Mice infected with virulent mouse-adapted severe acute respiratory

syndrome coronavirus (SARS-CoV) or Middle East respiratory syndrome coronavirus (MERS-CoV) have been similarly developed and are very useful for studies of pathogenesis, including in aged animals.

SARS, MERS and COVID-19 show age-dependent increases in severity¹. For example, no individual under the age of 24 years succumbed to SARS during the 2002–2003 epidemic, whereas 50% of those over 65 years died from the infection¹⁶. Parallel results were found in C57BL/6 mice infected with SARS. Young C57BL/6 mice were resistant to infection with mouse-adapted SARS but mice became progressively more susceptible beginning at about 5 months of age⁴. Poor survival correlated with a suboptimal T cell response, which resulted from delayed migration of respiratory dendritic cells to draining lymph nodes. We identified a single prostaglandin, PGD₂, that increased in the lungs during ageing and was responsible for impaired migration of dendritic cells⁴. We also showed that a single phospholipase A2 (PLA₂G2D) increased in

¹Department of Microbiology and Immunology, University of Iowa, Iowa City, IA, USA. ²BIOAGE Labs, Richmond, CA, USA. ³Department of Pediatrics, University of Iowa, Iowa City, IA, USA.

⁴Protein and Crystallography Facility, University of Iowa, Iowa City, IA, USA. ⁵Department Internal Medicine, University of Iowa, Iowa City, IA, USA. ⁶Department of Drug Discovery Medicine, Kyoto University, Kyoto, Japan. ⁷Center for Disease Biology and Integrative Medicine, Graduate School of Medicine, The University of Tokyo, Tokyo, Japan. ⁸Department of Molecular and Cell Biology, National Center of Biotechnology (CNB-CSIC), Campus Universidad Autónoma de Madrid, Madrid, Spain. ⁹Department of Pathology, University of Iowa, Iowa City, IA, USA. ¹⁰These authors contributed equally: Lok-Yin Roy Wong, Jian Zheng. ✉e-mail: paul-mccray@uiowa.edu; stanley-perlman@uiowa.edu

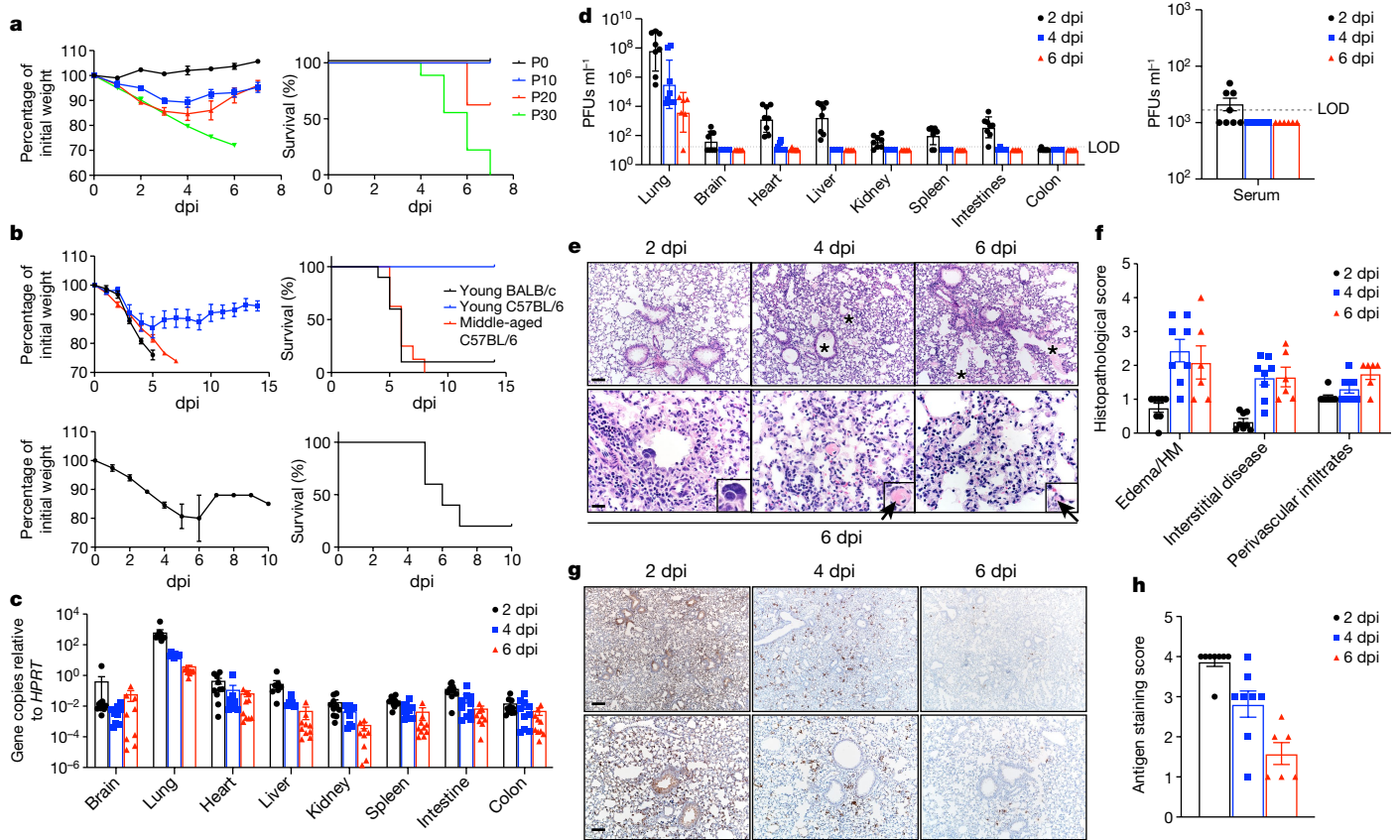


Fig. 1 | Clinical, virological and pathological disease in mice infected with SARS2-N501Y_{MA30}. **a**, Weight (left) and survival (right) of young BALB/c mice infected with passage (P) 0 ($n = 3$; 10^5 PFUs), P10 ($n = 8$; 9,000 PFUs), P20 ($n = 8$; 9,000 PFUs) or P30 ($n = 9$; 5,000 PFUs) SARS-CoV-2. P refers to the number of mouse lung passages. **b**, Weight (left panels) and survival (right panels) of young BALB/c ($n = 10$), young C57BL/6 ($n = 6$) or middle-aged C57BL/6 ($n = 8$) mice infected with 5,000 PFUs of SARS2-N501Y_{MA30} (upper panel). Weight (left) and survival (right) of middle-aged C57BL/6 ($n = 5$) mice infected with 5,000 PFUs of BAC-derived SARS2-N501Y_{MA30} (lower panel). Data are representative of two independent experiments. Data in **a** and **b** (left) are mean \pm s.e.m. **c**, **d**, Viral genomic RNA (**c**) and infectious viral titres (**d**) at 2, 4 and 6 dpi with 5,000 PFUs of SARS2-N501Y_{MA30} ($n = 10$ at all time points in **c**; $n = 8$ at 2 and 4 dpi, and $n = 6$ at 6 dpi in **d**). Serum titres are shown in the right panel of **d**. LOD, limit of detection.

Data in **c** and **d** are geometric mean \pm geometric s.d. **e–h**, Lungs from SARS2-N501Y_{MA30}-infected mice ($n = 8$ at 2 and 4 dpi; $n = 6$ at 6 dpi) were stained with haematoxylin and eosin (H&E) (**e**) or immunostained for SARS-CoV-2 nucleocapsid (**g**), and the pathological lesions and staining were quantified (**f** and **h**, respectively). **e**, Infected lungs exhibited airway edema (asterisks, top panels), multinucleated syncytial cells (inset in lower left panel), vascular thrombosis (arrows, insets in lower middle and right insets). Scale bars, 90 μ m (top) and 22 μ m (bottom); H&E stain. **f**, Summary scores of lung lesions ($n = 8$ at 2 and 4 dpi; $n = 6$ at 6 dpi). HM, hyaline membranes. **g**, Lungs from SARS2-N501Y_{MA30}-infected mice ($n = 8$ at 2 and 4 dpi; $n = 6$ at 6 dpi) were immunostained to detect SARS-CoV-2 nucleocapsid protein. Scale bars, 230 μ m (top) and 90 μ m (bottom). **h**, Summary scores of nucleocapsid immunostaining of lungs ($n = 8$ at 2 and 4 dpi; $n = 6$ at 6 dpi). Data in **f** and **h** are mean \pm sem.

mouse respiratory dendritic cells during ageing and was responsible for increased levels of PGD₂, as well as other prostaglandins in the aged mouse lung³. PGD₂ and PLA₂G2D seemed to increase during ageing partly in response to inflammaging and concomitant augmented oxidative stress³. Given the similarities between SARS, MERS and SARS-CoV-2 in age-dependent increased disease severity, we postulated that PGD₂ and PLA₂G2D would have similar roles in aged mice infected with a virulent strain of mouse-adapted SARS-CoV-2.

To generate a virulent mouse-adapted SARS-CoV-2, we inserted a sequence encoding the N501Y substitution into the SARS-CoV-2 genome (rSARS2-N501Y_{P0}) using reverse genetics as previously described¹⁷. As expected, this alteration rendered mice susceptible to SARS-CoV-2 infection, but BALB/c mice lost only a minimal amount of weight even after administration of 10^5 plaque-forming units (PFUs) of virus. After 30 passages through mouse lungs, the virus became highly virulent such that 5,000 PFUs caused a lethal disease in young BALB/c mice (Fig. 1a). We sequenced viruses after 10, 20 and 30 passages. Virus from these passages became progressively more lethal (Fig. 1a). Focusing on changes in the S protein, passage 10 virus contained a Q498R substitution, which probably enhanced binding to mACE2 (ref. 15; Fig. 2a, b). A similar substitution, Q498H, was identified in other mouse-adapted

SARS-CoV-2 strains^{18–20}. By passage 20, an alteration at position 493 (Q493R) was detected. By passage 30, alterations in residues 417 and 484 (K417M and E484K) also arose. E484K does not seem to be required for mouse virulence because it was variably expressed by different isolates that had equivalent lethality (Fig. 2d).

In silico modelling of the interaction between mACE2 and the S glycoprotein showed that Y501 in spike allowed π - π interactions and hydrophobic interactions with Y41 and H353 in mACE2, increasing the affinity and stability of the complex (Fig. 2c, e). Two additional spike substitutions (Q498R and Q493R) further increased affinity and stability, mainly driven by R493, which can create a salt bridge with D38 in mACE2 (previously a hydrogen bond between Q493 in spike and D38 in mACE2). Substitutions to other positively charged amino acids in residue 493 of spike have also been described in another mouse-adapted SARS-CoV-2 (ref. 15), suggesting the importance of this salt bridge to D38 in mACE2. The contribution of R498 in spike is probably due to an increase in the buried solvent-accessible surface area of this residue (from 80% to 99%), which improves the overall stability of the molecule and in turn could increase the affinity for mACE2. Residues K417 and E484 in spike do not interact directly with ACE2, and have been reported to have minimal effects on hACE2 binding²¹. E484K and

Article

various alterations in residue 417 have been associated with the variant of concern B.1.351 (E484K + K417N) and P.1 (E484K + K417T). Alterations in positions 417, 484, 493, 498 and 501 were detected in the variant of concern B.1.1.529 (Omicron variant). E484K and K417N have been shown to decrease antibody-mediated neutralization²² and therefore have been proposed to emerge in humans as an evolutionary advantage to evade immune responses. Here we show that E484K and alterations in K417 also occur in the absence of an adaptive immune response, offering an alternative explanation for the evolutionary pressures that drive the appearance of alterations in residues 417 and 484. Previously published models of murine SARS-CoV-2 have also reported substitutions at the same positions as the ones that we observed after 30 mouse lung passages^{15,18–20,23}, demonstrating the advantage of this particular combination of alterations in driving murine lethality.

Alterations in three nonstructural proteins, nsp4, nsp8 and nsp9, were detected at passage 20. T295I in nsp4 and T67A in nsp9 have been described in other models of SARS-CoV-2 mouse adaptation that caused moderate disease but were not lethal in young BALB/c mice¹⁵, suggesting that these alterations might be important in driving virulence but are insufficient to cause death. T67A in nsp9 has also been described in a lethal mouse model of SARS (ref.²⁴), suggesting that this alteration might be important for mouse adaptation not only in SARS-CoV-2 but also in other coronaviruses as well. To assess the importance of Q493R and the nsp alterations in virulence, we infected young BALB/c and middle-aged C57BL/6 mice with the B.1.351 strain, which contains K417N, E484K and N501Y. Infection with a high dose of virus (10^5 PFUs) resulted in modest weight loss and 20% lethality, indicating that one or more of the alterations detected in nsp4, nsp8, nsp9 and Q493R were required for mouse virulence (Fig. 2f).

Virus after 30 rounds of adaptation in mice was then plaque purified three times, and individual plaques were sequenced. One plaque was chosen for further study and propagated (SARS2-N501Y_{MA30}). Of note, SARS2-N501Y_{MA30} grew less well than rSARS2-N501Y_{P0} in human airway epithelial (Calu-3) cells, showing that increased virulence in mice did not result in increased replication in human cells (Extended Data Fig. 1a).

Clinical and pathological characterization

To further assess the virulence of SARS2-N501Y_{MA30}, we infected 6–10-week-old BALB/c and C57BL/6 mice and 6–9-month-old C57BL/6 mice intranasally with 5,000 PFUs (Fig. 1b). Administration of 5,000 PFUs of SARS2-N501Y_{MA30} caused a lethal infection in young BALB/c mice and middle-aged C57BL/6 mice but only modest weight loss in young C57BL/6 mice. To confirm that the alterations in SARS2-N501Y_{MA30} were sufficient to explain its virulence, we inserted all of the alterations into a bacterial artificial chromosome (BAC) cDNA clone. Virus rescued from this clone was lethal in 6–9-month-old C57BL/6 mice (Fig. 1b). For most of our subsequent experiments, we infected young BALB/c or middle-aged C57BL/6 mice with SARS2-N501Y_{MA30}. After infection of young BALB/c mice with 5,000 PFUs, viral genomic RNA was detected in most organs at all time points, although levels were much higher in the lungs (Fig. 1c). Infectious virus was detected in most organs at 2 days post infection (dpi), but by 4 and 6 dpi, it was detected only in the lungs and, to a lesser extent, the heart (Fig. 1d). Consistent with the presence of virus in organs, we also detected virus in the blood of 4 out of 8 mice at 2 dpi (Fig. 1d, right). To extend these results, we analysed histological samples for evidence of pathological changes and virus antigen (Fig. 1e–h). We detected pathological changes in the lungs and nasal cavity at all times, but not in other organs (Fig. 1e, f and Extended Data Figs. 1b, c and 2). Pathological findings in the lung included perivascular, peribronchial and interstitial infiltration and alveolar edema. We also detected occasional pulmonary vascular thrombi, which are prominent findings in patients with severe COVID-19 (ref.²⁵) and rare multinuclear syncytia (Fig. 1e, insets, bottom panels). In the sinonasal cavity, we detected evidence of infection of the olfactory and respiratory epithelium, with prominent infection of sustentacular

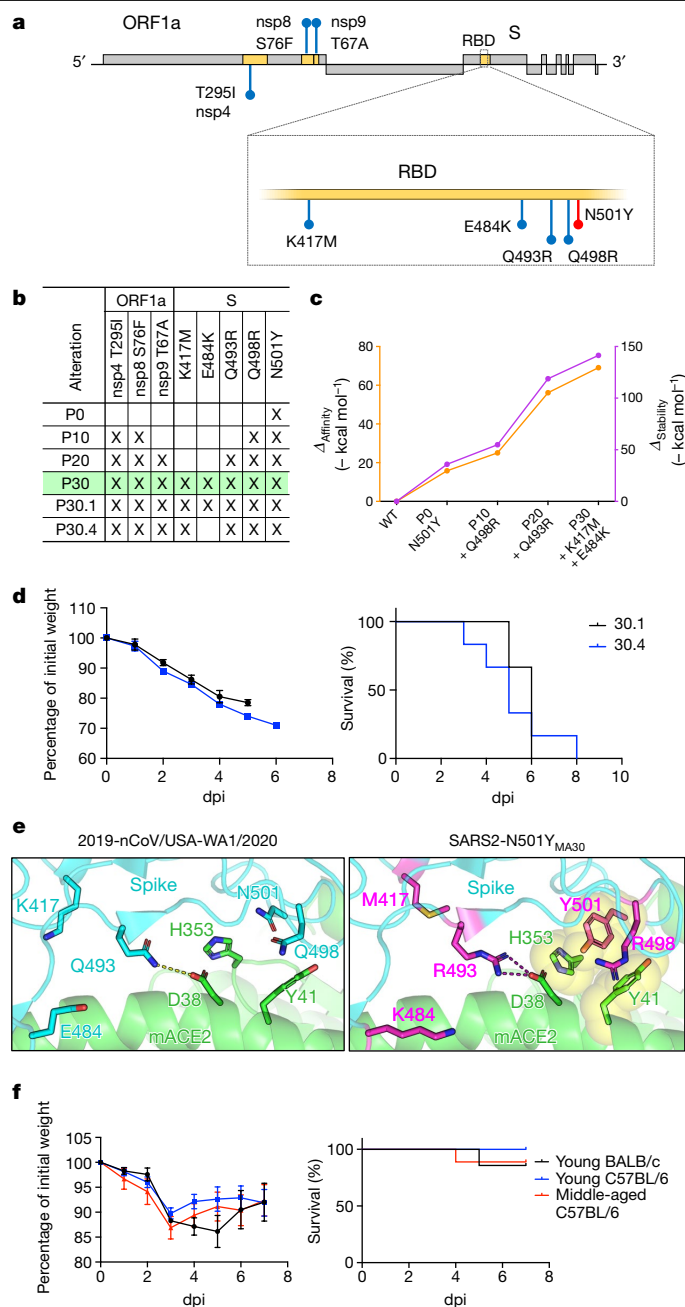


Fig. 2 | Analysis of alterations in SARS2-N501Y_{MA30} that arise during mouse adaptation. **a**, Schematic showing the genome of SARS-CoV-2. Initial N501Y alteration engineered into SARS-CoV-2 is shown in red. Viral proteins encoding alterations in SARS2-N501Y_{MA30} are shaded in yellow and the corresponding alterations are highlighted in blue. ORF1a, open reading frame 1a. **b**, Summary of alterations that emerged in different virus passages. P30 virus is highlighted in green. **c**, In silico modelling of the effects of alterations that emerged in serial mouse passaging on the affinity and stability of the S protein complexes with mACE2. **d**, Percentage of initial weight (left) and survival (right) of young BALB/c mice infected with viruses from two distinct plaque isolates purified from P30 virus. Virus from plaque 30.1 (black) encodes an extra alteration (E484K) in the S protein compared to virus from plaque 30.4 (blue) ($n = 6$ for both groups). **e**, Modelling of the receptor-binding interface between the S protein of 2019-nCoV/USA-WA1/2020 (left) and SARS2-N501Y_{MA30} (right) viruses and mACE2 reveals critical interactions mediated by alterations that emerged through serial passaging. **f**, Percentage of initial weight (left) and survival (right) of young BALB/c mice and young or old C57BL/6 mice infected with 10^5 PFUs of B.1.351 ($n = 7$ for young BALB/c; $n = 8$ for young C57BL/6; $n = 9$ for middle-aged C57BL/6). Data in **d** and **f** (left) are mean \pm s.e.m.

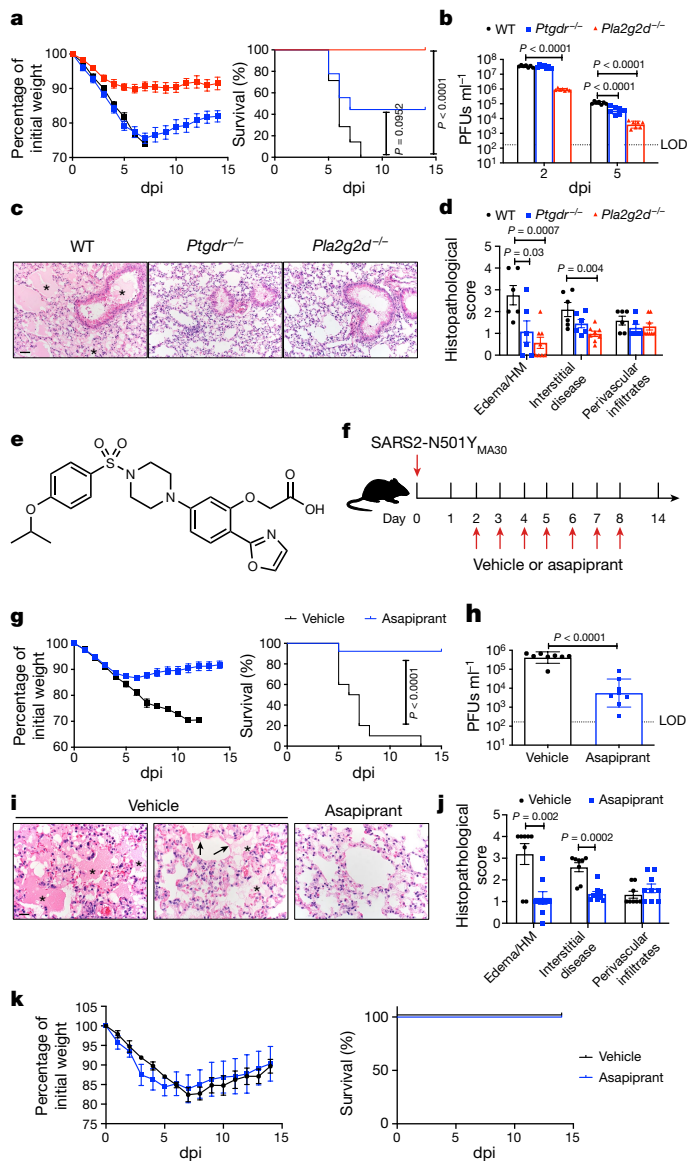


Fig. 3 | Absence of PLA₂G2D or PTGDR expression, or blocking PGD₂/PTGDR signalling, inhibits SARS2-N501Y_{MA30} infection in vivo. **a**, Weight (left) and survival (right) of middle-aged WT ($n = 8$), *Ptgdr*^{-/-} ($n = 9$) or *Pla2g2d*^{-/-} ($n = 9$) C57BL/6 mice infected with 5,000 PFUs of SARS2-N501Y_{MA30}. **b**, Viral titres in lungs at 2 ($n = 7$) and 5 dpi ($n = 7$). P values were determined by a log-rank (Mantel–Cox) test (**a**) and a two-tailed Student’s t -test (**b**). $P < 0.0001$, *Pla2g2d*^{-/-} versus WT; not significant, *Ptgdr*^{-/-} versus WT (**a**). $P < 0.0001$, *Pla2g2d*^{-/-} versus WT, 2 dpi; $P < 0.0001$, *Ptgdr*^{-/-} versus WT and *Pla2g2d*^{-/-} versus WT, 5 dpi (**b**). **c**, Lungs at 5 dpi from WT mice exhibited edema (marked with asterisks) and cellular infiltration/interstitial thickening whereas these were significantly reduced in lungs from *Ptgdr*^{-/-} or *Pla2g2d*^{-/-} mice. H&E stain. Scale bar, 40 μ m. **d**, Summary scores ($n = 6$ for WT; $n = 6$ for *Ptgdr*^{-/-}; $n = 8$ for *Pla2g2d*^{-/-}). P values were determined by two-tailed Student’s t -test. $P = 0.03$, *Ptgdr*^{-/-} versus WT and $P = 0.0007$, *Pla2g2d*^{-/-} versus WT, edema/HM; $P = 0.004$, *Pla2g2d*^{-/-} versus WT, interstitial disease. **e**, Asapiprant structure. **f**, Experimental design for **g** and **k**. Vehicle or asapiprant was administered orally at 2–8 dpi to middle-aged (**g–j**) or young (**k**) C57BL/6 mice infected intranasally with SARS2-N501Y_{MA30}. **g**, Weight (left) and survival (right) of vehicle-treated ($n = 10$) or asapiprant-treated ($n = 12$) middle-aged mice. The P value was determined by a two-tailed Student’s t -test. $P < 0.0001$, asapiprant-treated versus vehicle-treated group. **h**, Lung viral titres of vehicle-treated ($n = 8$) or asapiprant-treated ($n = 8$) middle-aged mice at 5 dpi. The P value was determined by a two-tailed Student’s t -test. $P < 0.0001$, asapiprant-treated versus vehicle-treated group. **i**, The vehicle-treated group exhibited edema (asterisks) with occasional hyaline membranes (arrows), which were uncommon in asapiprant-treated mice at 5 dpi; H&E stain. Scale bar, 20 μ m. **j**, Summary scores ($n = 8$ for vehicle-treated mice; $n = 9$ for asapiprant-treated mice). P values were determined by two-tailed Student’s t -test. $P = 0.002$, asapiprant-treated versus vehicle-treated group, edema/HM; $P = 0.0002$, asapiprant-treated versus vehicle-treated group, interstitial disease. HM, hyaline membranes. **k**, Weight (left) and survival (right) of vehicle-treated ($n = 4$) or asapiprant-treated ($n = 4$) young C57BL/6 mice infected with 5,000 PFUs of SARS2-N501Y_{MA30}. Data in **a**, **d**, **g** (left), **j** and **k** (left) are mean \pm s.e.m. Data in **b** and **h** are geometric mean \pm s.d.

cells (Extended Data Fig. 1b, c). Unlike in the case of SARS-CoV-2 infection of K18-hACE2 mice⁹, there was no pathological or immunohistochemical evidence of infection in the brain (Extended Data Fig. 1d, e).

Immunological responses

To further characterize the immunological response in the lungs to SARS2-N501Y_{MA30} infection, we measured the levels of several cytokines, chemokines and inflammation-associated molecules in BALB/c lungs at 2, 4 and 6 dpi. Mice were infected with 1,000 PFUs in these assays to ensure that most survived until 6 dpi. Increases in mRNA expression of interferons (IFNs; IFN α , IFN β , IFN γ and IFN λ), IFN-stimulated gene products (IFN-stimulated gene 15 and 2'-5'-oligoadenylate synthetase 1), cytokines (interleukin (IL)-1 α , IL-1 β , IL-6, IL-8, IL-12 and IL-15), chemokines (C-C motif chemokine ligand (CCL) 2, CCL5, C-X-C motif chemokine ligand (CXCL) 2, CXCL9 and CXCL10) and C-C motif chemokine receptor (CCR) 7, which is required for cell migration to draining lymph nodes, were observed over the course of the infection, with peak levels of IFN α , IFN β and IFN λ prominent at 2 dpi. (Extended Data Fig. 3a). Notably, levels of most of these pro-inflammatory molecules remained elevated throughout the infection, as also occurs in the blood of patients with COVID-19 (ref. 26). To determine the character of the cells infiltrating the lungs observed on pathological

examination, we immunophenotyped the infiltrating cells at 4 and 6 dpi (Extended Data Fig. 3b). Over time, there was a gradual increase in the numbers of infiltrating CD11b⁺ cells (macrophages, monocytes and neutrophils; Extended Data Fig. 3b). Virus-specific CD4⁺ and CD8⁺ T cells were detected in the lungs at 6 dpi and until at least 21 dpi. These cells expressed IFN γ and tumour necrosis factor (TNF) in response to stimulation with pools of peptides covering the SARS-CoV-2 structural proteins (spike, membrane and nucleocapsid) (Extended Data Fig. 3c–f). The S, N and M proteins all elicited CD4⁺ and CD8⁺ T cell responses, with the S protein responsible for the largest responses in both cell types. Lymphopenia and neutrophilia are hallmarks of severe COVID-19 (ref. 27) and were detected in middle-aged mice infected with SARS2-N501Y_{MA30} (Extended Data Fig. 4).

PGD₂ signalling and PLA₂G₂D expression

As we previously identified roles for PGD₂/PTGDR signalling and PLA₂G₂D expression by respiratory dendritic cells in enhanced disease in middle-aged mice infected with SARS (refs. 3,4), we next infected 8–12-month-old *Pla2g2d*^{-/-} and *Ptgdr*^{-/-} mice with 5,000 PFUs, a lethal dose of SARS2-N501Y_{MA30}. Lethality was completely or partially abrogated in the absence of PLA₂G₂D or PTGDR expression, respectively (Fig. 3a). In both cases, the kinetics of virus clearance was enhanced, probably contributing to diminished disease (Fig. 3b). Further, many of the pathological changes observed in the lungs of infected middle-aged C57BL/6 mice, such as extensive inflammatory infiltration and edema, were diminished in *Pla2g2d*^{-/-} and *Ptgdr*^{-/-} mice (Fig. 3c, d). Although the PLA₂G₂D–PGD₂/PTGDR pathway is generally anti-inflammatory, it contributes to the expression of TNF and other pro-inflammatory molecules in some settings^{28–30}. We assessed a possible pro-inflammatory role by measuring levels of several inflammatory mediators in WT and *Pla2g2d*^{-/-} and *Ptgdr*^{-/-} mice (Extended Data Fig. 5). In the absence of PTGDR expression, levels of IFN α , IFN β , IFN λ , CXCL10 and CCL2 all

increased, consistent with a predominant anti-inflammatory role for PGD₂/PTGDR signalling. By contrast, the absence of PLA₂G2D resulted in diminished expression of several molecules, including IL-2, CXCL2, CXCL9 and CCR7. The decreased expression of these molecules is expected to diminish the cellular inflammatory response and possibly decrease a potentially overly robust immune response. These differences in effects on inflammatory molecule expression may occur because the absence of PLA₂G2D affects not only PGD₂/PTGDR signalling but also the mobilization of omega-3 fatty acids^{31,32}. Together, these results show that PLA₂G2D, associated with poor outcomes in mice infected with SARS, also contributes to lethality in mice infected with SARS-CoV-2. The results also demonstrate that these pathological effects were at least partially mediated through the PGD₂/PTGDR axis.

Antagonizing PGD₂/PTGDR signalling

Although several drugs with inhibitory activity against PLA₂ molecules have been described³³, none is specific for murine PLA₂G2D. Next, we attempted to block PGD₂/PTGDR signalling using indomethacin, a non-steroidal anti-inflammatory drug (NSAID) inhibitor of cyclooxygenase 1 and 2. In addition, because prostaglandins are also involved in thrombus formation, NSAIDs, such as aspirin, might have a role in preventing their formation by inhibiting platelet-derived prostaglandin synthesis. However, clinical studies show that therapy with NSAIDs, including aspirin, are generally ineffective in ameliorating severe COVID-19 (refs. ^{34–38}). Consistent with these results, indomethacin treatment of infected mice resulted in no changes in morbidity and mortality (Extended Data Fig. 6a, b) probably because the production of all downstream lipid mediators is inhibited. However, aspirin ([2-(oxazol-2-yl)-5-(4-{4-[(propan-2-yl)oxy]phenylsulfonyl} piperazine-1-yl)phenoxy] acetic acid) (also known as BGE-175), a potent and specific antagonist of human PGD₂/PTGDR signalling with a mean inhibition constant *K*_i of 0.44 nM, has been described previously³⁹ (Fig. 3e). Asapirant affinity for PTGDR was 300- to >15,000-fold higher than for any other prostanoid receptor tested³⁹. We administered asapirant to middle-aged C57BL/6 mice by once daily oral gavage (30 mg kg⁻¹), starting at 2 dpi with 5,000 PFUs of SARS2-N501Y_{MA30} and for 6 days thereafter (Fig. 3f). We chose to start treatment at 2 dpi because this time is relevant for possible use in symptomatic patients. In middle-aged mice infected with a lethal dose of SARS2-N501Y_{MA30}, asapirant reduced mortality from 100% to <10%, with concomitant effects on weight loss (Fig. 3g). As expected on the basis of the studies of *Pla2g2d*^{-/-} and *Ptgdr*^{-/-} mice described above, drug treatment resulted in faster kinetics of virus clearance (Fig. 3h) and diminished pathological changes in the lungs (Fig. 3i, j). Asapirant also enhanced migration of respiratory dendritic cells from lungs infected with SARS2-N501Y_{MA30} to the draining mediastinal lymph nodes (Extended Data Fig. 6c) and reversed neutrophilia in the lungs and to a lesser extent in the blood (Extended Data Fig. 7). By contrast, treatment with the drug did not reduce the weight loss observed in young C57BL/6 mice infected with SARS2-N501Y_{MA30} (Fig. 3k). The effects of asapirant were not limited to SARS-CoV-2 infection because drug treatment 2 days after infection with SARS also prevented lethality (Extended Data Fig. 6e). The effects were specific for signalling through PTGDR because treatment with an antagonist of CRTH2 signalling (fevipiprant) did not improve outcomes (Extended Data Fig. 6d).

To understand the role of PLA₂G2D expression and PGD₂/PTGDR signalling in the clinical setting, we first analysed the literature for studies of age-dependent changes in lung levels of PGD₂ synthases (PGD₂ synthase (PTGDS) and haematopoietic prostaglandin D synthase), the enzymes required for conversion of prostaglandin H₂ to PGD₂, *Ptgdr* and *Pla2g2d* mRNA transcripts. Using RNA-sequencing data from 103 healthy lungs in a study of fibrosis⁴⁰ (Gene Expression Omnibus (GEO) accession GSE150910) and 578 lungs from the Genotype-Tissue Expression (GTEx) portal⁴¹, we found that levels of PTGDS and PTGDR increased with ageing (Fig. 4a, b). Next, we obtained peripheral blood

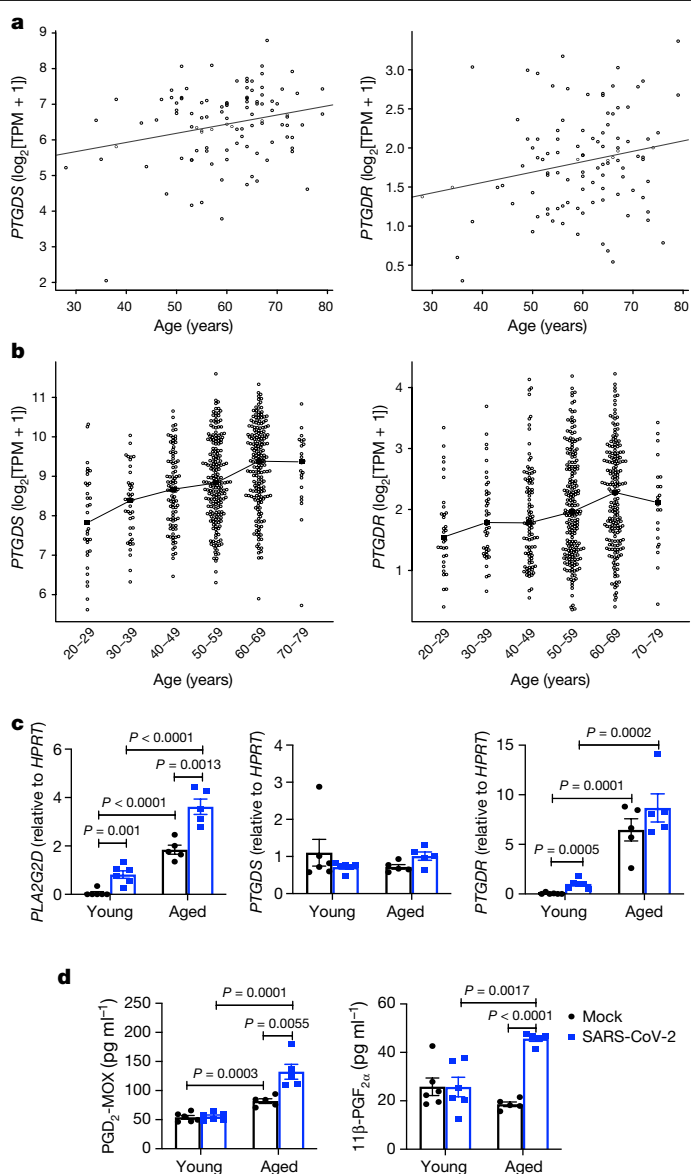


Fig. 4 | Expression of PTGDS, PTGDR, PLA₂G2D, PGD₂, and 11β-PGF_{2α} increases in human samples with age. **a, b**, Expression of PGD₂ genes (*PTGDS* (left panels) and *PTGDR* (right panels)) versus age in 103 healthy human lungs from GEO series GSE150910 (**a**) and 578 lungs from the GTEx project (**b**). The filled squares in **b** indicate the median expression for each age group. Expression levels of *PTGDS* and *PTGDR* were significantly associated with age in both studies (two-tailed Student's *t*-test *P* values *P* = 0.0108 and 0.0305, respectively, in **a**; analysis of variance *F*-test *P* values *P* < 0.0001 and 0.0028, respectively, in **b**). TPM, transcripts per million. **c**, Dendritic cells derived from peripheral blood mononuclear cells from 6 young (24–39 years, mean 29 years) and 5 aged (56–73 years, mean 62 years) donors were mock infected or infected with SARS-CoV-2. Cells and supernatants were collected at 5 dpi. RNA isolated from cells was assessed for transcript levels of the indicated genes. **d**, Levels of the indicated prostaglandins in cell supernatants measured by enzyme-linked immunosorbent assay. Data in **c, d** are mean ± s.e.m. *P* values determined by two-tailed Student's *t*-test (**c, d**).

mononuclear cells from young and aged human individuals and cultured them as described in the Methods to obtain dendritic cells. After 14 days, we infected these cells with SARS-CoV-2. SARS-CoV-2 causes an abortive infection of human dendritic cells⁴². We then measured mRNA expression levels of PLA₂G2D, PTGDR and PTGDS and cell supernatant levels of PGD₂-methoxime (PGD₂-MOX), a stabilized version of PGD₂, and 11β-prostaglandin F_{2α} (11β-PGF_{2α}), a PGD₂ enzymatic product. Expression of PLA₂G2D and PTGDR increased with ageing and that of PLA₂G2D

further increased after SARS-CoV-2 infection (Fig. 4c). PGD₂ increased with ageing and SARS-CoV-2 infection further enhanced expression by dendritic cells from aged individuals (Fig. 4d). 11β-PGF_{2α} increased in dendritic cells from aged people in response to infection (Fig. 4d).

Discussion

We describe a mouse-adapted SARS-CoV-2, isolated from mouse lungs after 30 serial passages. Unlike previously described mouse-adapted viruses, this strain is highly virulent in young and old mice, and infects only the lungs and not the brain. Further, it contains a set of alterations that are also observed in the B.1.351, P.1 and B.1.1.529 strains (K417N/T, E484K, Q493R, Q498R and N501Y) although K417N/T is replaced by K417M in SARS2-N501Y_{MA30}. All five amino acids are located in the receptor-binding domain, and E484 and N501 are hotspots for recognition by neutralizing antibodies²². Our results show that the selection of K417M (and by extension, presumably K417N) and E484K does not result solely from evasion of the antibody response because they arose in mice in the absence of any immune pressure. Infection of mice with B.1.351 resulted in mild disease, indicating that changes outside the S protein were critical for mouse virulence. T295I, located in the transmembrane domain of nsp4, and Q493K in the receptor-binding domain of S were identified in another variant of mouse-adapted SARS-CoV-2 (ref. ¹⁵) so alterations at these sites are prime candidates for conferring virulence in mice.

Our results identify a key role for PGD₂/PTGDR signalling in enhanced COVID-19 disease severity during ageing. We show that delivery of a PTGDR antagonist at 2 dpi, a time comparable to when drug might be used in patients, converted a lethal to a sublethal infection. Asapiprant has been used in previous studies of allergic rhinitis and asthma. In a rat model of asthma, oral asapiprant reduced inflammatory cell numbers in bronchoalveolar lavage fluid and reduced the increase in airway hyper-responsiveness³⁹. Asapiprant has been evaluated in 18 clinical studies (phases 1, 2 and 3) (2,000 patients and 200 healthy volunteers) conducted in the USA, the UK, France and Japan for the treatment of allergic rhinitis, alone or in combination with cetirizine, an anti-histamine⁴³. Once-daily dosing of asapiprant for up to 4 weeks was considered safe and well tolerated. Decreased airway resistance after PGD₂ challenge and decreased rhinitis symptom scores after allergen exposure were demonstrated in these studies, consistent with on-target pharmacodynamics⁴³. Asapiprant is now being used in randomized, placebo-controlled clinical trials of hospitalized individuals with COVID-19 who are at risk of respiratory failure (<https://clinicaltrials.gov/ct2/show/NCT04705597>). Together, our results show that infection of mice with SARS2-N501Y_{MA30} recapitulates many of the findings observed in patients with severe COVID-19 and also identify PGD₂/PTGDR signalling and PLA₂G2D as useful targets for therapy in aged individuals.

Online content

Any methods, additional references, Nature Research reporting summaries, source data, extended data, supplementary information, acknowledgements, peer review information; details of author contributions and competing interests; and statements of data and code availability are available at <https://doi.org/10.1038/s41586-022-04630-3>.

1. Channappanavar, R. & Perlman, S. Age-related susceptibility to coronavirus infections: role of impaired and dysregulated host immunity. *J. Clin. Invest.* **130**, 6204–6213 (2020).
2. Plante, J. A. et al. The variant gambit: COVID-19's next move. *Cell Host Microbe* **29**, 508–515 (2021).
3. Vijay, R. et al. Critical role of phospholipase A2 group IID in age-related susceptibility to severe acute respiratory syndrome-CoV infection. *J. Exp. Med.* **212**, 1851–1868 (2015).
4. Zhao, J., Zhao, J., Legge, K. & Perlman, S. Age-related increases in PGD₂ expression impair respiratory DC migration, resulting in diminished T cell responses upon respiratory virus infection in mice. *J. Clin. Invest.* **121**, 4921–4930 (2011).
5. Wan, Y., Shang, J., Graham, R., Baric, R. S. & Li, F. Receptor recognition by the novel coronavirus from Wuhan: an analysis based on decade-long structural studies of SARS coronavirus. *J. Virol.* **94**, e00127–20 (2020).
6. Bao, L. et al. The pathogenicity of SARS-CoV-2 in hACE2 transgenic mice. *Nature* **583**, 830–833 (2020).

7. Jiang, R. D. et al. Pathogenesis of SARS-CoV-2 in transgenic mice expressing human angiotensin-converting enzyme 2. *Cell* **182**, 50–58 (2020).
8. Winkler, E. S. et al. SARS-CoV-2 infection of human ACE2-transgenic mice causes severe lung inflammation and impaired function. *Nat. Immunol.* **21**, 1327–1335 (2020).
9. Zheng, J. et al. COVID-19 treatments and pathogenesis including anosmia in K18-hACE2 mice. *Nature* **589**, 603–607 (2021).
10. Sun, S. H. et al. A mouse model of SARS-CoV-2 infection and pathogenesis. *Cell Host Microbe* **28**, 124–133 (2020).
11. Hassan, A. O. et al. A SARS-CoV-2 infection model in mice demonstrates protection by neutralizing antibodies. *Cell* **182**, 744–753 (2020).
12. Sun, J. et al. Generation of a broadly useful model for COVID-19 pathogenesis, vaccination, and treatment. *Cell* **182**, 734–743 (2020).
13. Dinnon, K. H. III et al. A mouse-adapted model of SARS-CoV-2 to test COVID-19 countermeasures. *Nature* **586**, 560–566 (2020).
14. Gu, H. et al. Adaptation of SARS-CoV-2 in BALB/c mice for testing vaccine efficacy. *Science* **369**, 1603–1607 (2020).
15. Leist, S. R. et al. A mouse-adapted SARS-CoV-2 induces acute lung injury and mortality in standard laboratory mice. *Cell* **183**, 1070–1085 (2020).
16. Peiris, J. S., Guan, Y. & Yuen, K. Y. Severe acute respiratory syndrome. *Nat. Med.* **10**, S88–S97 (2004).
17. Fehr, A. R. Bacterial artificial chromosome-based lambda red recombination with the I-SceI homing endonuclease for genetic alteration of MERS-CoV. *Methods Mol. Biol.* **2099**, 53–68 (2020).
18. Huang, K. et al. Q493K and Q498H substitutions in Spike promote adaptation of SARS-CoV-2 in mice. *EBioMedicine* **67**, 103381 (2021).
19. Wang, J. et al. Mouse-adapted SARS-CoV-2 replicates efficiently in the upper and lower respiratory tract of BALB/c and C57BL/6J mice. *Protein Cell* **11**, 776–782 (2020).
20. Zhang, Y. et al. SARS-CoV-2 rapidly adapts in aged BALB/c mice and induces typical pneumonia. *J. Virol.* **95**, e02477–20 (2021).
21. Starr, T. N. et al. Deep mutational scanning of SARS-CoV-2 receptor binding domain reveals constraints on folding and ACE2 binding. *Cell* **182**, 1295–1310 (2020).
22. Li, Q. et al. SARS-CoV-2 501Y.V2 variants lack higher infectivity but do have immune escape. *Cell* **184**, 2362–2371 (2021).
23. Sun, H. et al. Characterization and structural basis of a lethal mouse-adapted SARS-CoV-2. *Nat. Commun.* **12**, 5654 (2021).
24. Roberts, A. et al. A mouse-adapted SARS-coronavirus causes disease and mortality in BALB/c mice. *PLoS Pathog.* **3**, e5 (2007).
25. Ackermann, M. et al. Pulmonary vascular endothelialitis, thrombosis, and angiogenesis in Covid-19. *N. Engl. J. Med.* **383**, 120–128 (2020).
26. Galani, I. E. et al. Untuned antiviral immunity in COVID-19 revealed by temporal type I/III interferon patterns and flu comparison. *Nat. Immunol.* **22**, 32–40 (2021).
27. Zhang, X. et al. Viral and host factors related to the clinical outcome of COVID-19. *Nature* **583**, 437–440 (2020).
28. Hirano, Y. et al. Synergistic effect of PGD₂ via prostanoid DP receptor on TNF-α-induced production of MCP-1 and IL-8 in human monocyte THP-1 cells. *Eur. J. Pharmacol.* **560**, 81–88 (2007).
29. Hirano, Y. et al. Prostanoid DP receptor antagonists suppress symptomatic asthma-like manifestation by distinct actions from a glucocorticoid in rats. *Eur. J. Pharmacol.* **666**, 233–241 (2011).
30. Ullah, M. A., Ritchie, S., Li, J., Hasnain, S. Z. & Phipps, S. DP1 prostanoid receptor activation increases the severity of an acute lower respiratory viral infection in mice via TNF-α-induced immunopathology. *Mucosal Immunol.* **14**, 963–972 (2021).
31. Miki, Y. et al. Dual roles of group IID phospholipase A2 in inflammation and cancer. *J. Biol. Chem.* **291**, 15588–15601 (2016).
32. Miki, Y. et al. Lymphoid tissue phospholipase A2 group IID resolves contact hypersensitivity by driving antiinflammatory lipid mediators. *J. Exp. Med.* **210**, 1217–1234 (2013).
33. Oslund, R. C., Cermak, N. & Gelb, M. H. Highly specific and broadly potent inhibitors of mammalian secreted phospholipases A2. *J. Med. Chem.* **51**, 4708–4714 (2008).
34. Drake, T. M. et al. Non-steroidal anti-inflammatory drug use and outcomes of COVID-19 in the ISARIC Clinical Characterisation Protocol UK cohort: a matched, prospective cohort study. *Lancet Rheumatol.* **3**, e498–e506 (2021).
35. RECOVERY Collaborative Group. Aspirin in patients admitted to hospital with COVID-19 (RECOVERY): a randomised, controlled, open-label, platform trial. *Lancet* [https://doi.org/10.1016/S0140-6736\(21\)01825-0](https://doi.org/10.1016/S0140-6736(21)01825-0) (2021).
36. Kragholm, K., Torp-Pedersen, C. & Fosbol, E. Non-steroidal anti-inflammatory drug use in COVID-19. *Lancet Rheumatol.* **3**, e465–e466 (2021).
37. Santoro, F. et al. Antiplatelet therapy and outcome in COVID-19: the Health Outcome Predictive Evaluation Registry. *Heart* <https://doi.org/10.1136/heartjnl-2021-319552> (2021).
38. Voruganti, D., Bassareo, P. P., Calcaterra, G. & Mehta, J. L. Does aspirin save lives in patients with COVID-19? *Heart* <https://doi.org/10.1136/heartjnl-2021-320255> (2021).
39. Takahashi, G. et al. Effect of the potent and selective DP1 receptor antagonist, asapiprant (S-555739), in animal models of allergic rhinitis and allergic asthma. *Eur. J. Pharmacol.* **765**, 15–23 (2015).
40. Furusawa, H. et al. Chronic hypersensitivity pneumonitis, an interstitial lung disease with distinct molecular signatures. *Am. J. Respir. Crit. Care Med.* **202**, 1430–1444 (2020).
41. Carithers, L. J. & Moore, H. M. The Genotype-Tissue Expression (GTEx) Project. *Biopreserv. Biobank.* **13**, 307–308 (2015).
42. Zheng, J. et al. Severe acute respiratory syndrome coronavirus 2-induced immune activation and death of monocyte-derived human macrophages and dendritic cells. *J. Infect. Dis.* **223**, 785–795 (2021).
43. Marone, G. et al. Prostaglandin D2 receptor antagonists in allergic disorders: safety, efficacy, and future perspectives. *Expert Opin. Investig. Drugs* **28**, 73–84 (2019).

Publisher's note Springer Nature remains neutral with regard to jurisdictional claims in published maps and institutional affiliations.

© The Author(s), under exclusive licence to Springer Nature Limited 2022

Methods

Generation of SARS-CoV-2 encoding N501Y alteration in the S protein and recombinant SARS2-N501Y_{MA30}

p-BAC SARS-CoV-2 carrying the sequence of the isolate Wuhan-Hu-1 (WT-SARS-CoV-2 BAC) was constructed on the basis of a previously described method⁴⁴. The only difference between the Wuhan-Hu-1 and 2019n-CoV/USA-WA1/2019 strains is one amino acid change in ORF8 and 2 silent alterations (in ORF1a and ORF1b). Two silent alterations were introduced into the BAC clone to enable differentiation from wild-type SARS-CoV-2 (A20085G and G26840C). p-BAC SARS-CoV-2 with a N501Y substitution in spike (N501Y-SARS-CoV-2 BAC) or mouse-adapted alterations were generated using a lambda red recombination system with I-SceI homing endonuclease as previously described¹⁷. To generate N501Y-SARS-CoV-2 BAC, forward and reverse primers with overlapping SARS-CoV-2 spike sequence with the N501Y alteration followed by sequence complementary to the target plasmid (pEP-KanS) were synthesized (Invitrogen). A PCR fragment with overlapping ends carrying SARS-CoV-2 sequence flanking the kanamycin-resistance marker was amplified with the primers described using pEP-KanS as template. The PCR fragment was purified using a gel purification kit (Invitrogen). Purified PCR fragment was electroporated into GS1783 strains of *Escherichia coli* carrying p-BAC SARS-CoV-2. Successful recombinants were selected with kanamycin resistance. The kanamycin marker was removed by arabinose induction of I-SceI cleavage followed by homologous recombination of the overlapping ends. Successful recombinants were selected by replica plating for the loss of kanamycin resistance. Recombinants were purified and sequenced to confirm the introduction of alteration into the BAC clone. The primer sequences used to introduce the N501Y alteration are as follows: forward, 5'-CCTTGTAAATGGTGTGAAGGTTTAAATTGTTACTTTCCTTTACAATCATAT

GGTTTCCAACCCACTTATGGTGTGGTTAGGATGACGACGATAAGTAG-3'; reverse, 5'-CATGTAGAAGTCAAAAAGAAAGTACTACTACTCTGATGGTTGGTAACCAACA

CCATTAGTGGTGGTAAACCATCAACCAATTAACCAATTCTGATTAG-3'. For generation of SARS2-N501Y_{MA30}, four substitutions (E484K, Q493R, Q498R and N501Y) in the S protein (4S) were introduced in a single round of recombination, followed by the K417M substitution in the S protein, the nsp4 (T295I) substitution and transcriptional regulatory sequence (TRS) alteration of the M protein (A26058G). The nsp8 (S76F) and nsp9 (T67A) alterations were introduced using CRISPR-Cas9 editing as described in the following section. The primer sequences used for the 4S alterations are as follows: forward, 5'-CGGTAGCACACTTGTAAATGGTGTAAAGGTTTAAATTGTTACTTTCCTTTA

CGATCATATGGTTCGACCCACTTATGAGGATGACGACGATAAGTAG-3'; reverse, 5'-GTATGGTGGTAACCAACACCATAAGTGGTTCGAAACCATATGATCGTAA

GGAAAGTAACAATTAACCTTTCAACCAATTAACCAATTCTGATTAG-3'. The primer sequences used for the K417M alteration are as follows: forward, 5'-GAGGTGATGAAGTCAGACAAATCGCTCCAGGGCAAACCTGGAATGATTGCT

GATTATAATTATAAAAGGATGACGACGATAAGTAG-3'; reverse, 5'-CAGCTGTAAAATCATCTGGTAATTATAATTATAATCAGCAATCATTTCA

GTTTGCCTGGAGCGATCAACCAATTAACCAATTCTGATTAG-3'. The primer sequences used for the nsp 4 alteration are as follows: forward, 5'-GACATATCAGCATCTATAGTAGCTGGTGGTATTGTAGCTATCGTAGTATATGCTTGGCTACTATTTTATGAGAGGATGACGACGATAAGTAG-3'; reverse, 5'-CACAAAAGCTCTTCTAAACCTATAAAATAGTAGGCAAGCATATTACT

ACGATAGCTACAATACCAACCAATTAACCAATTCTGATTAG-3'. The primer sequences used for the TRS alteration of the M protein are as follows: forward, 5'-CTGGTCTAAACGAACTAAATATATATTAGTTTTCTGTTGGAGCTTTAA

TTTTAGCCATGGCAGAAGGATGACGACGATAAGTAG-3'; reverse, 5'-CAACGGTAATAGTACCCTGGAAATCTGCCATGGCTAAAATTAAGCTCAAACAGAAAACTAATAATCAACCAATTAACCAATTCTGATTAG-3'. Base changes are shown in italics; sequences complementary to pEP-KanS are shown in bold.

Next, the nsp8 (S76F) and nsp9 (T67A) alterations of SARS2-N501Y_{MA30} were introduced using CRISPR-Cas technology to generate a BAC cDNA clone with a full set of SARS2-N501Y_{MA30} alterations. The alteration-encoding PCR product was linked and amplified from two PCR fragments with either the nsp8 or the nsp9 alteration by two-step PCR. Guide RNAs targeting the desired cleavage site were designed using online resources (<https://chopchop.cbu.uib.no>). DNA oligonucleotide sequences were generated with the EnGen sgRNA template oligonucleotide designer (NEB; <https://sgRNA.neb.com/#!/sgRNA>) to include essential elements for guide RNA transcription and RNA scaffold for Cas9 recognition. DNA oligonucleotides were chemically synthesized and transcribed with an EnGen sgRNA synthesis kit (NEB) according to the manufacturer's protocol. sgRNAs were purified using Monarch kits for RNA cleanup (NEB). CRISPR-Cas9 cleavage was performed according to the manufacturer's protocol (NEB). Cleaved BAC products were recovered by gel purification using the PureLink Quick Gel Extraction and PCR Purification Combo Kit (Invitrogen). Purified BAC products were incubated with alteration-encoding PCR products for in vitro recombination with Gibson assembly (NEB) according to the manufacturer's protocol. Ligation products were transformed into DH10β cells. Bacterial colonies derived from the ligation products were cultured for DNA extraction to isolate mutant BACs. Introduction of alterations was verified by Sanger sequencing. Oligonucleotide sequences for sgRNAs are as follows: sgRNA1, 5'-TTCTAATACGACTC ACTATAGTTAGATATATGAATTCACAGTTT TAGA

GCTAGA-3'; sgRNA2, 5'-TTCTAATACGACTCACTATAGTCTGTAACAACCTACAAGGGTTTT

AGAGCTAGA-3'. Target DNA sequences are underlined. Primer sequences for amplifying PCR product encoding the nsp8 alteration are as follows: forward, 5'-ACAGGAGTTAGATATATGAATTCACAGGGAC-3'; reverse, 5'-GTCCTCAAATCTAGCCTGTTTA-3'. Primer sequences for amplifying PCR product encoding the nsp9 alteration are as follows: forward, 5'-TAAACAGGCTAGATTTGAGGAC-3'; reverse, 5'-GTGTGTCTGTAACAAACCTACAAGGTGGTTCAGTTCTGCATAGAT-3'. Base changes are indicated in bold.

A 2 μg quantity of mutant BACs was transfected into Vero E6 cells (ATCC) with Lipofectamine 3000 (Invitrogen) in a 6-well plate according to the manufacturer's protocol. Cells were monitored daily for cytopathic effects (CPEs). Cultures were collected when the CPE was >50% by freezing at -80 °C. rSARS2-N501Y_{p0} and rSARS2-N501Y_{MA30} were further passaged in Calu-3 cells in DMEM supplemented with 20% fetal bovine serum (FBS). Virus titres were determined by plaque assay.

Mice, cells and virus

BALB/c and C57BL/6 mice of 6–10 weeks or 6 months of age were obtained from Charles River Laboratories. Mice were maintained in the Animal Care Unit at the University of Iowa under standard conditions of dark/light cycle, ambient temperature and humidity. Mice were randomly assigned to different groups, with numbers per group sufficient to obtain statistical significance. 2019-nCoV/USA-WA1/2020 (accession number MN985325.1) and 20H/501Y.V2 (B.1.351, BEI catalogue number NR-54009) were obtained from BEI and passaged in Calu-3 2B4 cells⁴⁵. Calu-3 2B4 cells were grown in Dulbecco's modified Eagle's medium (DMEM, GIBCO) supplemented with 20% FBS. Vero E6 cells (ATCC CRL-1586) were grown in DMEM supplemented with 10% FBS. All viruses were sequenced after propagation and found to match the input strain.

Serial in vivo passaging of virus in mice

Serial blind passage of rSARS2-N501Y_{p0} through mouse lungs was performed in 8–10-week-old BALB/c mice. In brief, two mice were

each inoculated with 50 µl of the virus intranasally at each passage. At 2/3 dpi, mice were euthanized, and lungs were pooled, homogenized in PBS and used to infect naive mice. After 30 passages, virus was obtained and plaque purified three times using Vero E6 cells. Several isolates were obtained and a single one was chosen for further study (SARS2-N501Y_{MA30}). SARS2-N501Y_{MA30} was further propagated in Calu-3 2B4 cells.

Mouse infection

Mice were anaesthetized with ketamine–xylazine and infected intranasally with the indicated amount of virus in a total volume of 50 µl DMEM. Animal weight and health were monitored daily. All experiments with SARS-CoV-2 were performed in a biosafety level 3 (BSL3) laboratory at the University of Iowa. All animal studies were approved by the University of Iowa Animal Care and Use Committee and meet stipulations of the Guide for the Care and Use of Laboratory Animals.

Virus titre by plaque assay

At the indicated times, mice were euthanized and transcardially perfused with PBS. Organs were collected and homogenized before clarification by centrifugation and titring. Virus or tissue homogenate supernatants were serially diluted in DMEM. Twelve-well plates of VeroE6 cells were inoculated at 37 °C in 5% CO₂ for 1 h and gently rocked every 15 min. After removing the inocula, plates were overlaid with 0.6% agarose containing 2% FBS. After 3 days, overlays were removed, and plaques visualized by staining with 0.1% crystal violet. Viral titres were quantified as PFUs per ml tissue.

Collection of whole blood/serum

Mice were anaesthetized by intraperitoneal injection of ketamine–xylazine. Blood was collected through retro-orbital bleed with a capillary tube (Fisher Scientific). Blood was allowed to clot at room temperature for 30 min. Serum was clarified by centrifugation and transferred to a new tube for storage at –80 °C. For collection of whole blood, heparinized capillary tubes were used (Fisher Scientific).

Histology and immunohistochemistry

Mice were anaesthetized by intraperitoneal injection of ketamine–xylazine and perfused transcardially with PBS. Tissues were fixed in zinc formalin. For routine histology, tissue sections (≈4 µm each) were stained with H&E. Tissues were evaluated for the presence of edema or hyaline membranes (0–4) using distribution-based ordinal scoring: 0, none; 1, <25%; 2, 26–50%; 3, 51–75%; 4, >75% of tissue fields. Perivascular lymphoid inflammation was evaluated by severity-based ordinal scoring: 0, absent; 1, minor (solitary to loose infiltration of cells); 2, moderate (small to medium aggregates); 3, severe (robust aggregates that are circumferential around vessels and can extend into adjacent parenchyma). Interstitial scores were evaluated using a modified H score for the presence of interstitial disease: 0, none; 1, minor (increased cellularity in septa); 2, moderate (cellular infiltrates with some thickened septa and uncommon inflammatory cells extending into lumen); 3, severe (cellular infiltrates in thickened septa and filling in air-space lumens with atelectasis and/or evidence of diffuse alveolar damage (edema or hyaline membranes)). For each score, this was multiplied by the percentage of lung affected, and then summed for each lung and divided by 100 to yield a final score of 0–3. For SARS-CoV-2 antigen detection, slides were incubated with blocking reagent (10% normal goat serum for 30 min) followed by rabbit monoclonal antibody against SARS-CoV-2 N protein (1:20,000 dilution for 60 min, number 40143-R019, Sino Biological), and then incubated with rabbit Envision (Dako) and diaminobenzidine (Dako) as chromogen. Lung tissue sections were evaluated by a boarded veterinary pathologist familiar with the model using the post-examination method of masking⁴⁶. IHC was ordinally scored on the percentage distribution of staining in the tissues: 0, absent; 1, 0–25%; 2, 26–50%; 3, 51–75%; 4, >75% of tissue.

Lung cell preparation and antibodies for flow cytometric analysis

Animals were anaesthetized with ketamine–xylazine and perfused transcardially with 10 ml PBS. Lungs were removed, minced and digested in HBSS buffer consisting of 2% fetal calf serum, 25 mM HEPES, 1 mg ml⁻¹ collagenase D (Roche) and 0.1 mg ml⁻¹ DNase (Roche) at 37 °C for 30 min. Single-cell suspensions were prepared by passage through a 70-µm cell strainer. Cells were enumerated with a Scepter 2.0 cell counter (MilliporeSigma). Whole blood was treated with ACK lysis buffer for 1 min. Cells were washed and pelleted. Cells were then washed and blocked with 1 µg anti-CD16/anti-CD32 (2.4G2) at 4 °C for 20 min and surface stained with the following antibodies at 4 °C for 30 min: V450 anti-mouse CD45 (clone 30-F11; catalogue number 560501); APC anti-mouse CD220 (clone RA3-6B2, catalogue number 553092); APC/cyanine 7 anti-mouse CD3e (clone 145-2C11, catalogue number 100330); APC/cyanine 7 anti-mouse CD11c (clone HL3; catalogue number 561241); FITC anti-mouse Ly6G (clone 1A8; catalogue number 127606); PE anti-mouse CD11b (clone M1/70; catalogue number 101208); PE/cyanine 7 anti-mouse CD8 (clone 53-6.7; catalogue number 100722); PerCP/cyanine 5.5 anti-mouse CD4 (clone RM4.5; catalogue number 550954); FITC anti-mouse Ly6G (1A8; catalogue number 127606); PerCP/cyanine 5.5 anti-mouse Ly6C (clone HK1.4; catalogue number 128012); CD64 (clone X54-5/7.1; catalogue number 139304). All antibodies were used at 1:200 dilution. Cells were washed, fixed and permeabilized with Cytotfix/Cytoperm (BD Biosciences). The gating strategy is shown in Supplementary Fig. 1.

For intracellular cytokine staining (ICS), lymphocytes were cultured in 96-well dishes at 37 °C for 5–6 h in the presence of 2 µM peptide pool and brefeldin A (BD Biosciences). Cells were then labelled for cell-surface markers, fixed/permeabilized with Cytotfix/Cytoperm Solution (BD Biosciences) and labelled with anti-IFN γ and anti-TNF (1:100 dilution). All flow cytometry data were acquired using a BD FACVerse and analysed with FlowJo software.

RNA isolation and RT-qPCR

Total RNA was extracted from tissues using TRIzol (Invitrogen) or a Direct-zol RNA Miniprep kit (Zymo Research) according to the manufacturer's protocol. Following DNase treatment, 200 ng of total RNA was used as a template for first-strand cDNA using a High-Capacity cDNA Reverse Transcription Kit (Applied Biosystems). The resulting cDNA was subjected to amplification of selected genes by real-time quantitative PCR using Power SYBR Green PCR Master Mix (Applied Biosystems). Average values from duplicates of each gene were used to calculate the relative abundance of transcripts normalized to *HPRT* and presented as 2^{- Δ CT}. The primers used for cytokine and chemokines were reported previously⁴⁷. For detection of viral genomes, the following primers were used to amplify the genomic RNA for the N protein: 2019-nCoV_N1-F: 5'-GACCCCAAATCAGCGAAAT-3'; 2019-nCoV_N1-R: 5'-TCTGGTTACTGCCAGTTGAATCTG-3'. The following primers were used to amplify the subgenomic RNA for the E protein: F, 5'-CGATCTCTGTAGATCTGTTCTC-3'; R, 5'-ATATTGCA CGAGTACGCACACA-3'.

Viral whole-genome sequencing

Samples were treated with TRIzol reagent for viral inactivation and RNA extraction. Sequencing libraries were prepared using the sequencing protocol (v2) and primer pools (v3) from the ARTIC network (<https://doi.org/10.17504/protocols.io.bdp7i5rn>). Reads were sequenced on a MinION sequencer from Oxford Nanopore Technologies and consensus sequences were generated using Medaka following the ARTIC network nCoV-2019 bioinformatics protocol v1.1.0 (<https://artic.network/ncov-2019/ncov2019-bioinformatics-sop.html>). A total of 249,944 average reads \pm 82,509 (standard deviation) was obtained per sample. After quality filtering and alignment, the average sequencing depth was >200 \times per amplicon for each sample. The consensus sequence of P10 and P20 virus from mouse lung homogenates contained areas with

Article

low sequencing depth; to accurately cover these gaps, we amplified the missing regions using individual PCR reactions and performed Sanger sequencing on the amplicons.

In silico structural modelling and analysis

A homology model for mACE2 (NP_001123985.1) was generated using YASARA and docked into the crystal structure of complexed hACE2 and spike RBD (PDB: 6M0J). Alteration calculations were performed on the mACE2–spike complex in Bioluminate (Schrodinger Release 2020-4) by first using the Protein Preparation Wizard and then the Residue Scanning module. Stability and affinity calculations were performed optimizing for the affinity, and backbone minimization was used with a cutoff of 5 Å. Figures were generated in PyMOL. Software used was installed and configured by SBGrid (ref. 48).

Treatment with indomethacin, asapiprant and fevipiprant. Male and female 7–8-month-old C57BL/6 mice were infected with SARS2-N501Y_{MA30} (5,000 PFUs). For indomethacin treatment, mice were treated daily from days 0–4 or 2–6 after infection with 0.2 ml PBS or 10 mg kg⁻¹ indomethacin diluted in 0.2 ml PBS. For asapiprant treatment, mice were treated daily at 2–8 dpi with 0.2 ml vehicle (0.5% carboxymethylcellulose sodium (NaCMC), Sigma) or 30 mg kg⁻¹ asapiprant (BioAge). For fevipiprant treatment, mice were treated with 5 mg kg⁻¹ fevipiprant (Medkoo) diluted in 0.2 ml vehicle twice daily. Drugs and vehicle/PBS were administered through oral gavage.

Generation of human dendritic cells. Human peripheral blood cells were obtained from anonymous donors at the DeGowin Blood Center at the University of Iowa. Consent forms were approved by the University of Iowa Institutional Review Board. To obtain monocytes, peripheral blood mononuclear cells were isolated by density gradient centrifugation through Ficoll-Paque PLUS density gradient medium (Cytiva) and cultured at a seeding density of 1×10^6 cells ml⁻¹ in RP-10 medium (RPMI-1640 medium (Invitrogen) supplemented with 10% FBS (Atlanta Biologicals)), 2 mM L-glutamine and 100 ng ml⁻¹ granulocyte macrophage colony-stimulating factor (PeproTech) + 50 ng ml⁻¹ IL-4 (PeproTech) at 37 °C for 96 h. Plates were then washed with Hanks' balanced salt solution lacking divalent cations (Invitrogen) to remove non-adherent cells. Adherent cells were then trypsinized, pelleted and cultured for 10 days.

Statistics and reproducibility

Differences in mean values between groups were analysed by analysis of variance and Student's *t*-tests and differences in survival were analysed by log-rank (Mantel–Cox) tests using Microsoft Excel and GraphPad Prism 8. All results are expressed as mean ± s.e.m. and were corrected for multiple comparisons. $P < 0.05$ was considered statistically significant.

The data in Figs. 1, 2d, f and 3 were pooled from two independent experiments, except for those in Fig. 3k, which shows representative data from two independent experiments. The data in Fig. 3c, i are representative of two independent experiments with similar results.

Reporting summary

Further information on research design is available in the Nature Research Reporting Summary linked to this paper.

Data availability

The data supporting the findings of this study are documented within the paper and are available from the corresponding authors upon request. Human datasets were obtained from the GEO accession GSE150910 and the GTEx portal (<https://www.gtexportal.org/home/>) for analysis. The sequence of the mouse-adapted virus was deposited in GISAID (<https://www.gisaid.org/>) (accession ID EPI_ISL_1666328). Source data are provided with this paper.

- Almazan, F. et al. Engineering a replication-competent, propagation-defective Middle East respiratory syndrome coronavirus as a vaccine candidate. *MBio* **4**, e00650–13 (2013).
- Yoshikawa, T. et al. Dynamic innate immune responses of human bronchial epithelial cells to severe acute respiratory syndrome-associated coronavirus infection. *PLoS ONE* **5**, e8729 (2010).
- Meyerholz, D. K. & Beck, A. P. Principles and approaches for reproducible scoring of tissue stains in research. *Lab. Invest.* **98**, 844–855 (2018).
- Li, K. et al. Middle East respiratory syndrome coronavirus causes multiple organ damage and lethal disease in mice transgenic for human dipeptidyl peptidase 4. *J. Infect. Dis.* **213**, 712–722 (2016).
- Morin, A. et al. Collaboration gets the most out of software. *Life* **2**, e01456 (2013).

Acknowledgements This work is supported in part by grants from the National Institutes of Health USA (NIH; P01 AI060699 (S.P. and P.B.M.) and R01 AI129269 (S.P.)) and BIOAGE Labs (S.P.). The Pathology Core is partially supported by the Center for Gene Therapy for Cystic Fibrosis (NIH grant P30 DK-54759) and the Cystic Fibrosis Foundation. P.B.M. is supported by the Roy J. Carver Charitable Trust. L.-Y.R.W. is supported by Mechanism of Parasitism Training Grant (T32 AI007511). We thank M. Gelb (University of Washington) for *Pla2g2d*^{-/-} mice.

Author contributions experiments, and contributed to data interpretation and manuscript preparation. J.Z. and K.L. contributed to experimental design, data interpretation and manuscript preparation. K.W. contributed to experimental design, manuscript writing and data interpretation. M.E.O. performed the sequence analyses and modelling and contributed to manuscript preparation. N.J.S. performed in silico modelling and analysis. A.T. performed data analysis. A.A.P. performed sequence and data analyses. P.J.S. performed sequence analysis. P.L. and R.P. constructed recombinant mouse-adapted virus. K.K., F.A. and J.R. contributed to experimental design, manuscript preparation and data interpretation. S.N., M.M., S.Z., I.S. and L.E. provided critical reagents. D.K.M. analysed and scored the pathological sections. K.F. contributed to manuscript preparation. P.B.M. designed experiments and contributed to data interpretation and manuscript preparation. S.P. designed and coordinated the study, designed experiments and contributed to data interpretation, data presentation and manuscript preparation.

Competing interests K.W., K.K., F.A., J.R. and K.F. are employees of BIOAGE Labs. All other authors have no competing interests.

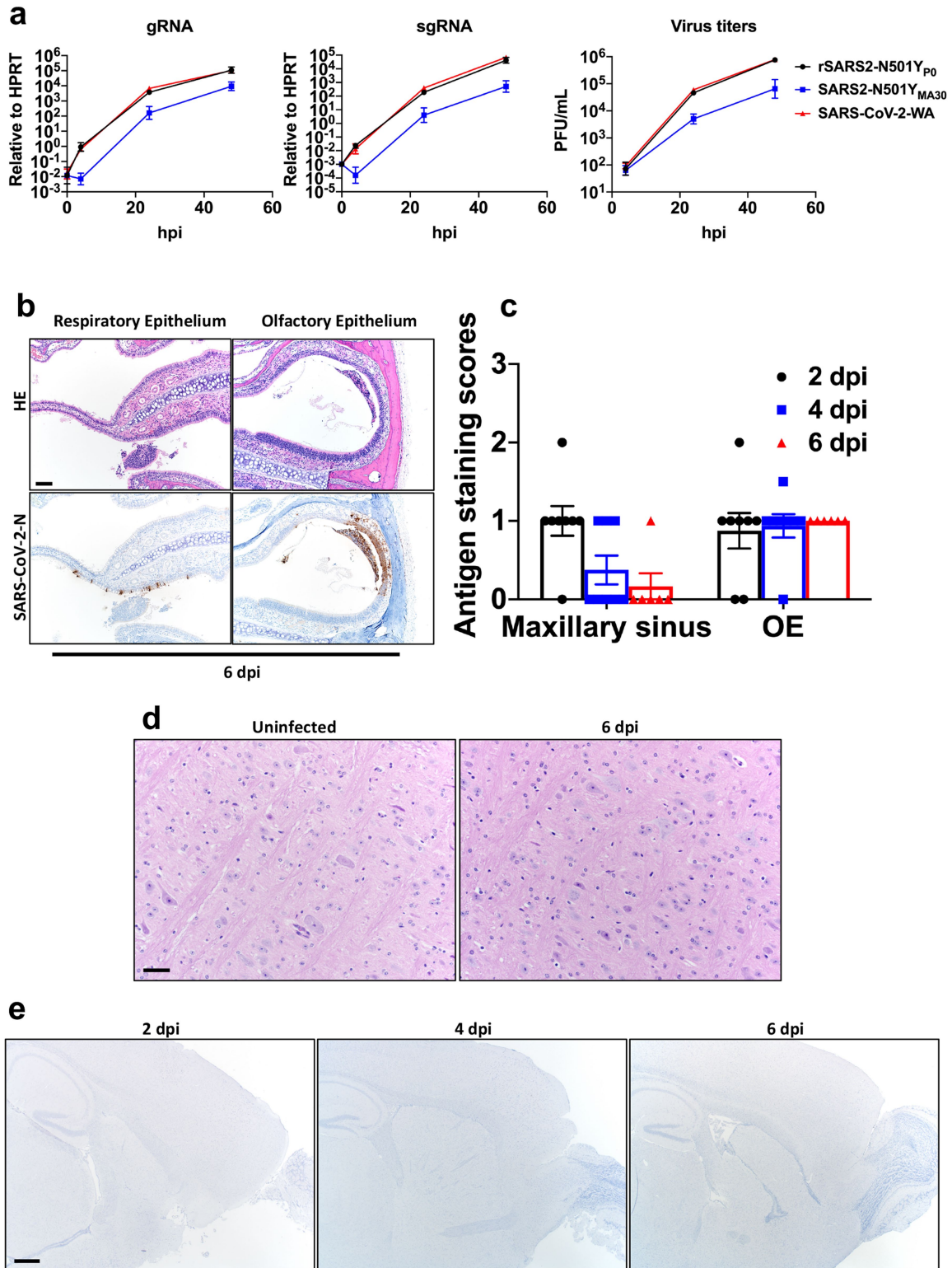
Additional information

Supplementary information The online version contains supplementary material available at <https://doi.org/10.1038/s41586-022-04630-3>.

Correspondence and requests for materials should be addressed to Paul B. McCray or Stanley Perlman.

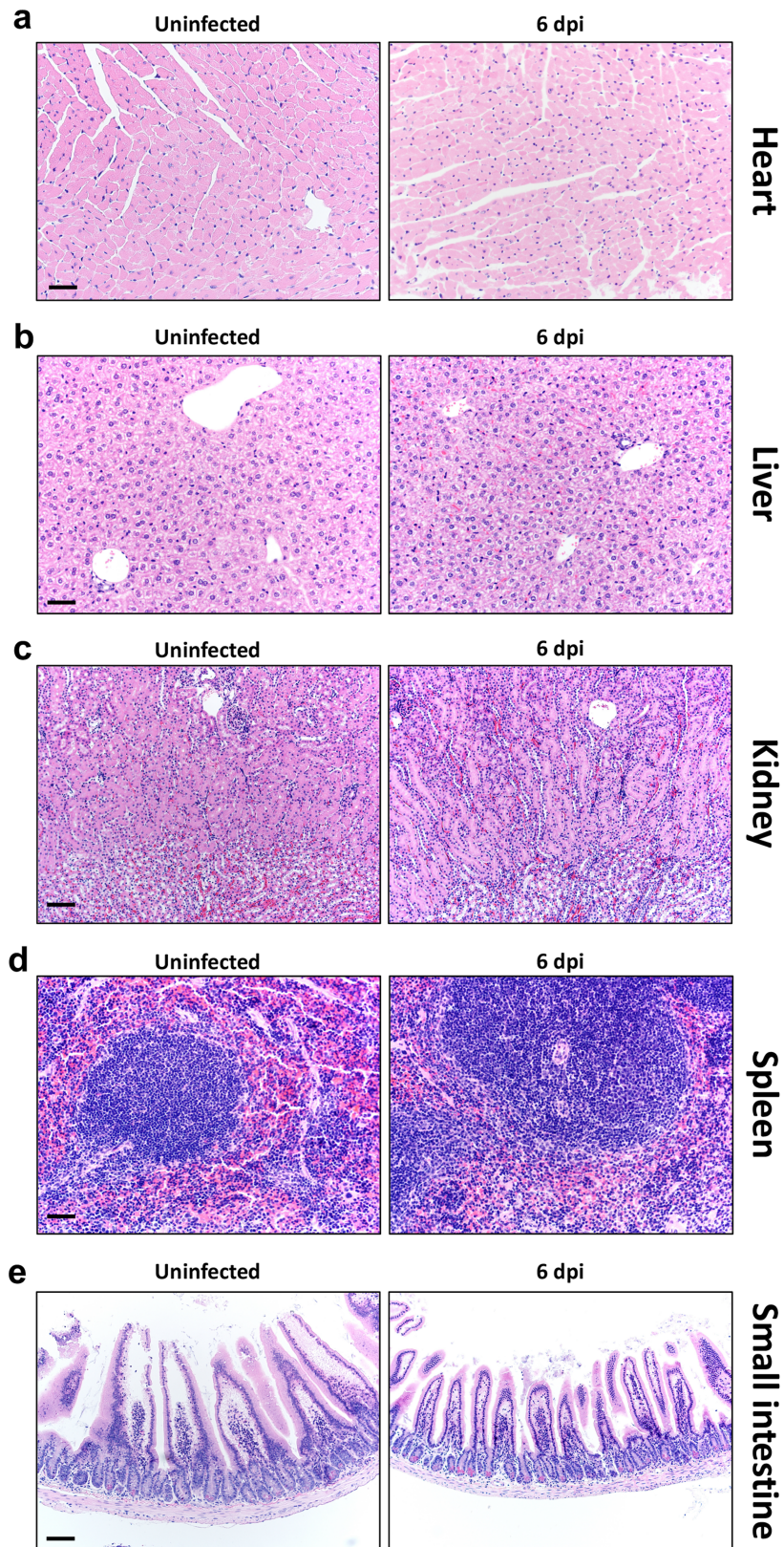
Peer review information Nature thanks Lisa Gralinski and the other, anonymous, reviewer(s) for their contribution to the peer review of this work.

Reprints and permissions information is available at <http://www.nature.com/reprints>.



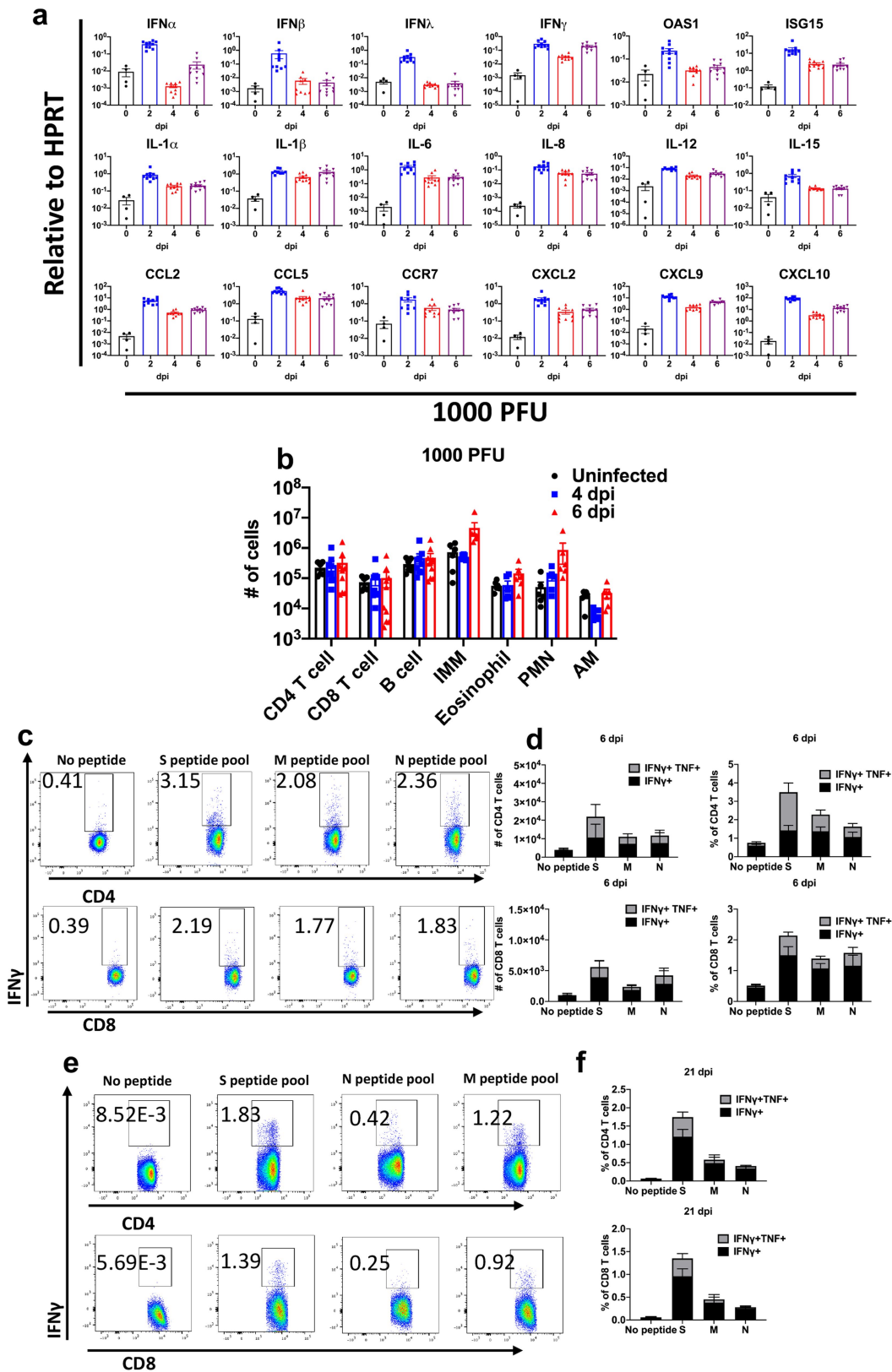
Extended Data Fig. 1 | Infection of human respiratory cells and distribution of SARS2-N501Y_{MA30} antigen in sinonasal cavity and brain. **a**, Quantification of genomic RNA (gRNA), subgenomic RNA (sgRNA) and virus titers in Calu-3 cells at the indicated times after infection with 0.01 MOI of the indicated viruses. Data in **a** are geometric mean \pm geometric SD and are representative of two independent experiments. **b**, Sinonasal cavity from young BALB/c mice infected with 5000 PFU of SARS2-N501Y_{MA30}, H&E stain (top panels). Regions of respiratory epithelium and olfactory epithelium exhibited uncommon regional scattered (bottom-left panel) to localized SARS-CoV-2 nucleocapsid

immunostaining, (bottom panels). Scale bar 90 μ m. OE: olfactory epithelium. **c**, Summary scores of nucleocapsid staining, as described in Methods (n = 8 at 2, 4 dpi; n = 6 at 6 dpi). Data in **c** are mean \pm s.e.m. **d**, Brains from uninfected or infected young BALB/c mice at 6 dpi lacked overt lesions, H&E stain. Scale bar 45 μ m. **e**, Brains from uninfected mice or young BALB/c mice infected with 5000 PFU at 2, 4, and 6 dpi revealed no SARS-CoV-2 nucleocapsid immunostaining. Scale bar 460 μ m. Data were pooled from two independent experiments. Data in **b**, **d** are representative of two independent experiments with similar results.



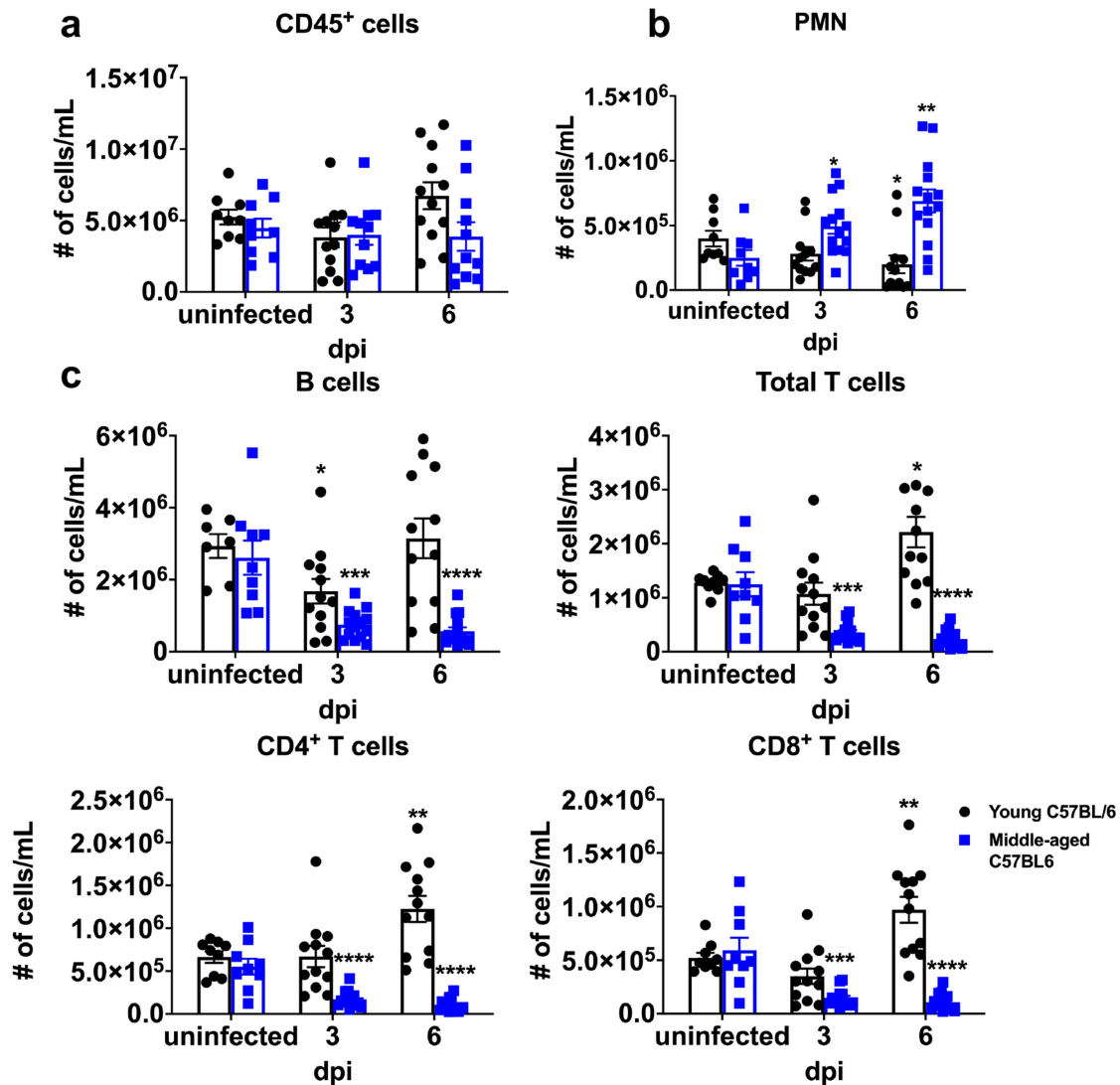
Extended Data Fig. 2 | Histological analysis of extrapulmonary tissue. Mice infected with 5000 PFU of SARS2-N501Y_{MA30} were sacrificed at 6 dpi with 5000 PFU of SARS2-N501Y_{MA30} and tissues were prepared for histological examination. Tissues from uninfected mice were analyzed in parallel. **a–e**, heart (**a**), liver (**b**),

kidney (**c**), spleen (**d**), and small intestine (**e**) were studied. No overt, group-specific lesions were observed. Scale bars, 45 μ m (**a**, **b**, **d**) and 90 μ m (**c**, **e**), H&E stain. Two sections of each organ from 6 mice per group were evaluated. Representative images from two independent experiments are shown.



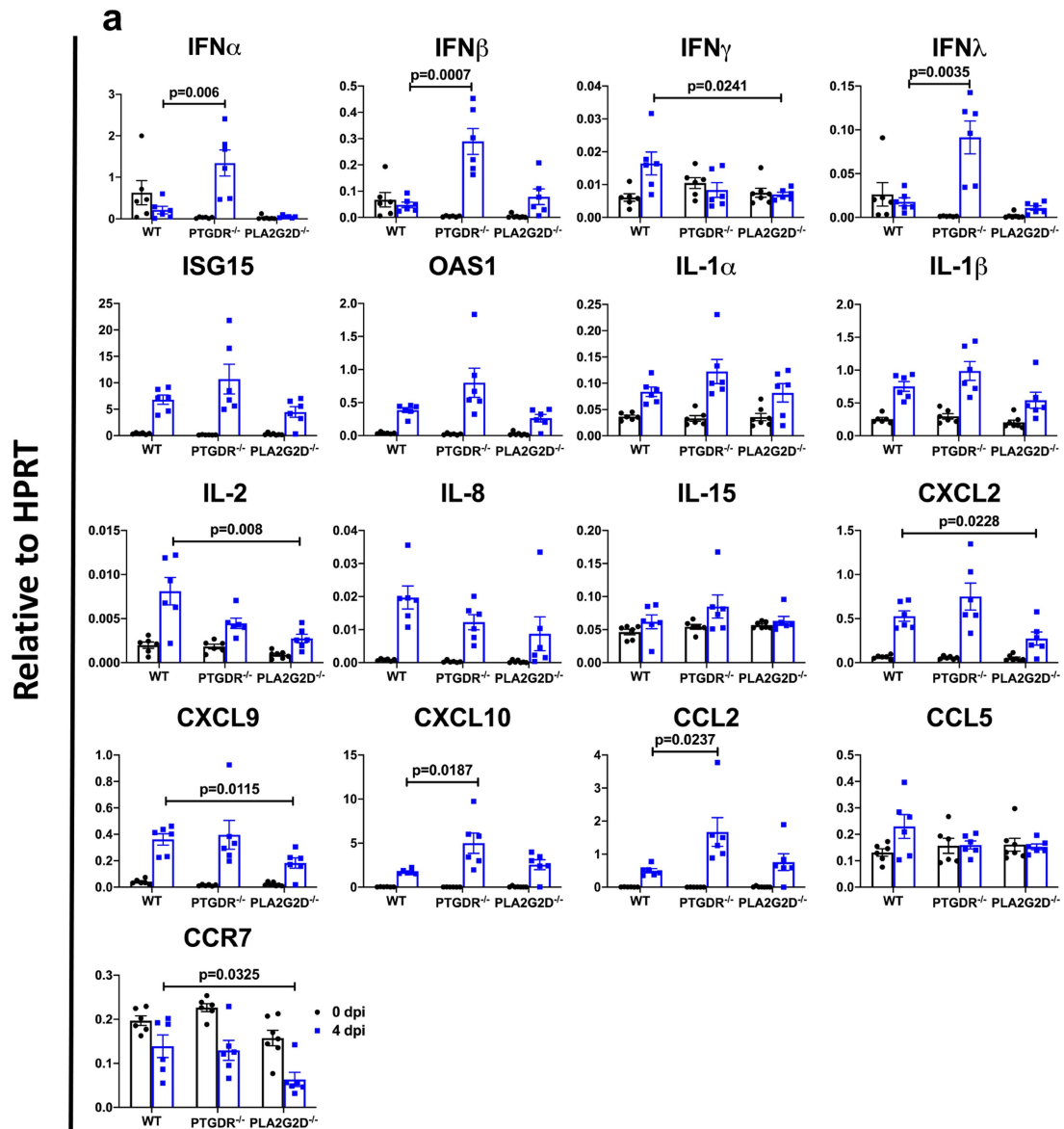
Extended Data Fig. 3 | Inflammatory mediators and immune effector cells in infected lungs. Mice were infected with 1000 PFU SARS2-N501Y_{MA30} to ensure survival until 6 dpi. **a**, Cytokine and chemokine transcripts were measured by qRT-PCR after isolation of RNA from the lungs of uninfected (0 dpi) and infected young BALB/c mice. Each lung was collected from an individual mouse. Mock (0 dpi), $n = 4$; 2, 4, and 6 dpi, $n = 10$. **b**, Quantification of immune cells (as gated in Supplementary Fig. 1) in the lungs ($n = 6$ for uninfected group; $n = 9$ for CD4, CD8 and B cells; $n = 6$ for IMM, eosinophils,

PMNs and AM, for both 4 and 6 dpi) each lung was collected from an individual mouse). IMM: inflammatory monocytes/macrophages; PMN: neutrophils; AM: alveolar macrophages. **c, e**, Representative FACS plots of IFN γ ⁺ CD4⁺ and CD8⁺ T cells after stimulation with indicated peptide pools in the lungs of young BALB/c mice at 6 (**c**) and 21 (**e**) dpi. **d, f**, Summary data for IFN γ and TNF expression are shown ($n = 5$, 6 dpi; $n = 4$, 21 dpi). Data in **a, b, d** are mean \pm s.e.m. **a** and **b** are pooled data from two independent experiments. Data in **c-f** are from one of two independent experiments.



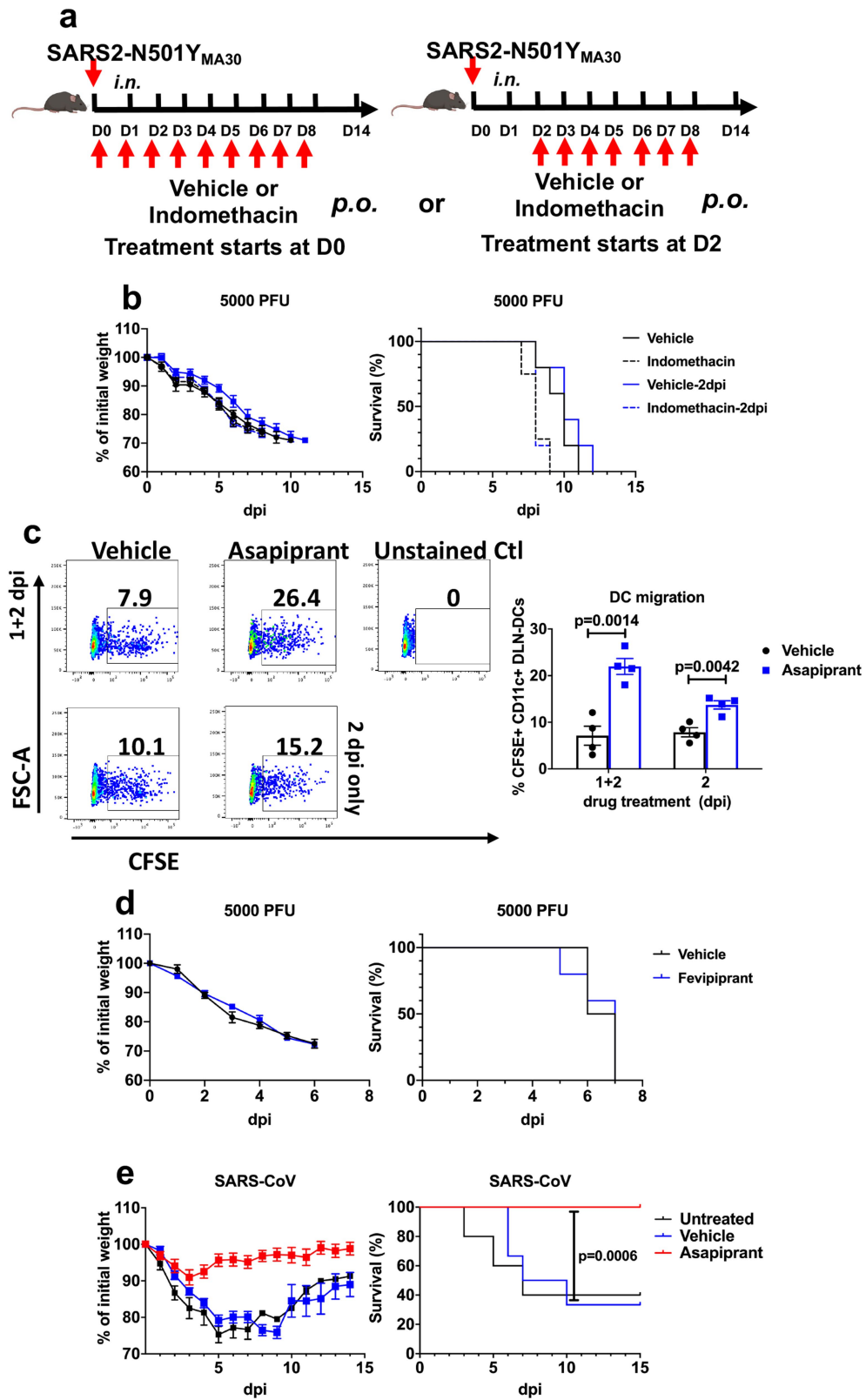
Extended Data Fig. 4 | Lymphopenia in SARS2-N501Y_{MA30}-infected middle-aged mice. Numbers of immune cells in the blood of young and middle-aged C57BL/6 mice at 3 and 6 days after infection with 5000 PFU of SARS2-N501Y_{MA30} (n = 9 for uninfected controls in both groups; n = 14 for middle-aged mice at 3 and 6 dpi; n = 12 for young mice at 3 and 6 dpi). **a.** CD45⁺ cells; **b.** PMN: Polymorphonuclear cells. **c.** B and T cells. *P* values determined by two-tailed Student's *t* test. *P* values indicated are determined from the corresponding time point compared to uninfected control of the same group. *P* = 0.0483 (6 dpi vs uninfected, young C57BL/6; PMN); *P* = 0.0117 (3 dpi vs uninfected, middle-aged C57BL/6, PMN); *P* = 0.0016 (6 dpi vs uninfected, middle-aged C57BL/6, PMN); *P* = 0.0264 (3 dpi vs uninfected, young C57BL/6; B cells);

P = 0.0001 (3 dpi vs uninfected, 6 dpi vs uninfected middle-aged C57BL/6, B cells); *P* = 0.0109 (6 dpi vs uninfected, young C57BL/6; Total T cells); *P* = 0.0001 (3 dpi vs uninfected, middle-aged C57BL/6, Total T cells); *P* < 0.0001 (6 dpi vs uninfected, middle-aged C57BL/6, Total T cells); *P* = 0.0072 (6 dpi vs uninfected, young C57BL/6; CD4⁺ T cells); *P* < 0.0001 (3 dpi vs uninfected, 6 dpi vs uninfected, middle-aged C57BL/6, CD4⁺ T cells); *P* = 0.0065 (6 dpi vs uninfected, young C57BL/6; CD8⁺ T cells); *P* = 0.0001 (3 dpi vs uninfected, middle-aged C57BL/6, CD8⁺ T cells); *P* < 0.0001 (6 dpi vs uninfected, middle-aged C57BL/6, CD8⁺ T cells). **P* ≤ 0.05, ***P* ≤ 0.01, ****P* ≤ 0.001, *****P* ≤ 0.0001. Data in **a** are mean ± s.e.m. Data are pooled from two independent experiments.



Extended Data Fig. 5 | Cytokine and chemokine expression profile in middle-aged WT, PTGDR^{-/-} or PLA₂G2D^{-/-} C57BL/6 mice after SARS2-N501Y_{MA30} infection. a. Middle-aged WT, PTGDR^{-/-} and PLA₂G2D^{-/-} C57BL/6 mice were infected with 5000 PFU SARS2-N501Y_{MA30}. Cytokine and chemokine

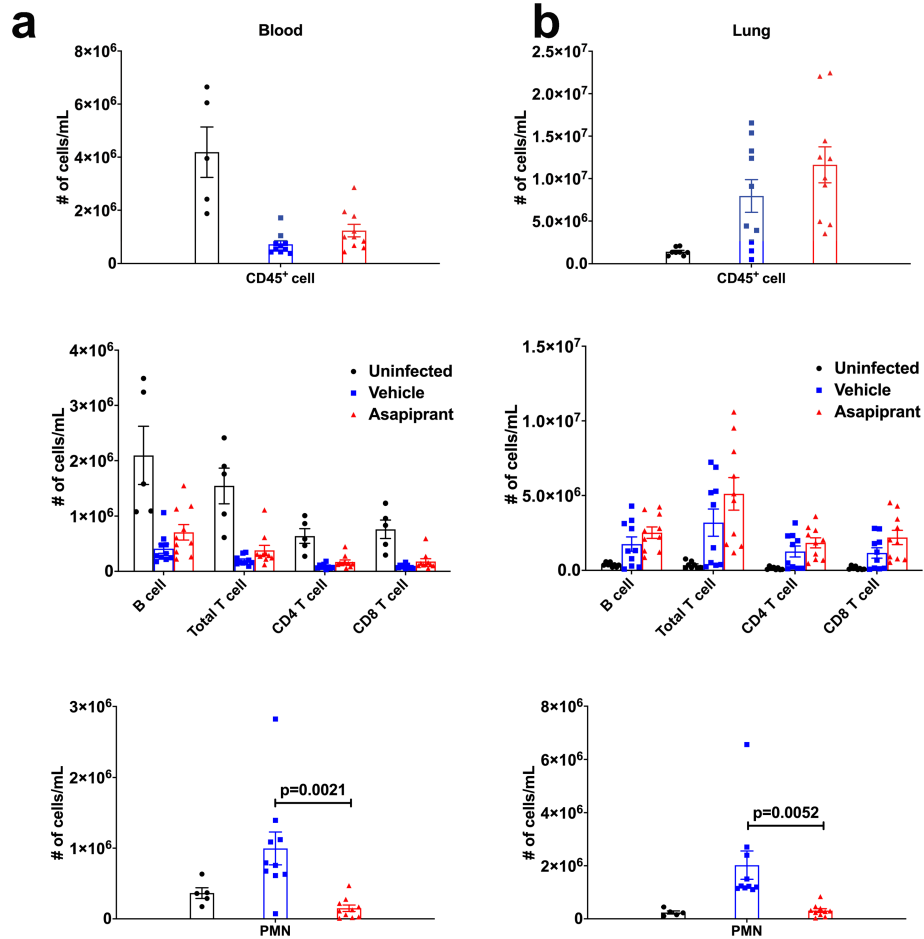
transcripts were detected by qRT-PCR from the lungs of uninfected (0 dpi) and infected mice at 4 dpi. Each lung was collected from an individual mouse. $n = 6$ for all groups at 0 and 4 dpi except for PLA₂G2D^{-/-} mice at 0 dpi where $n = 7$. Data are mean \pm s.e.m. Data are pooled from two independent experiments.



Extended Data Fig. 6 | See next page for caption.

Extended Data Fig. 6 | Effects of asapiprant, indomethacin and fevipiprant in aged mice infected with SARS-CoV-2 or SARS-CoV. a, Schematic showing experimental design for results shown in panel **b** (mouse image with BioRender.com). **b**, Percentage of initial weight and survival of middle-aged C57BL/6 mice infected with 5000 PFU of SARS2-N501Y_{MA30} after indomethacin treatment (n = 5 in all groups except in the group when indomethacin was given at 0 dpi, where n = 4). **c**, Middle-aged C57BL/6 mice were instilled with CFSE intranasally 6 h before infection with 5000 PFU of SARS2-N501Y_{MA30}. One group of mice received vehicle or asapiprant at 1 and 2 dpi (1+2) while another group of mice received drug treatment only at 2 dpi (2). Mice were euthanized at 3 dpi and lung draining lymph node (DLN; mediastinal) were harvested and analyzed with flow

cytometry. rDC migration from the lung to DLN was measured as the frequency of CFSE⁺CD11c⁺ cells in the DLN (n = 4). **d**, Percentage of initial weight and survival of middle-aged C57BL/6 mice infected with 5000 PFU of SARS2-N501Y_{MA30} with fevipiprant (CRTH2 inhibitor) treatment (two times a day; days 2 to 8; 5 mg/kg) (n = 4, vehicle; n = 5, fevipiprant). **e**, Percentage of initial weight and survival of middle-aged C57BL/6 mice infected with 10⁴ PFU of SARS-CoV, with vehicle or asapiprant treatment from day 2 to 8 (n = 5, untreated; n = 12, vehicle and asapiprant). *P* values determined by two-tailed Student's *t* test in **a** and log-rank (Mental-Cox) in **e**. Data are mean ± s.e.m. and are representative of at least two independent experiments.



Extended Data Fig. 7 | Asapiprant reversed neutrophilia but not lymphopenia in infected mice. Numbers of immune cells in the blood (a) and lung (b) of middle-aged C57BL/6 mice at 6 days after infection with 5000 PFU of SARS2-N501Y_{MA30} with vehicle or asapiprant treatment starting at 2 dpi (n = 5 for

uninfected controls; n = 10 vehicle- and asapiprant-treated mice). PMN: Polymorphonuclear neutrophils. *P* values determined by two-tailed Student's *t* test. Data are mean ± s.e.m. Data are pooled from two independent experiments.

Reporting Summary

Nature Research wishes to improve the reproducibility of the work that we publish. This form provides structure for consistency and transparency in reporting. For further information on Nature Research policies, see our [Editorial Policies](#) and the [Editorial Policy Checklist](#).

Statistics

For all statistical analyses, confirm that the following items are present in the figure legend, table legend, main text, or Methods section.

n/a Confirmed

- The exact sample size (n) for each experimental group/condition, given as a discrete number and unit of measurement
- A statement on whether measurements were taken from distinct samples or whether the same sample was measured repeatedly
- The statistical test(s) used AND whether they are one- or two-sided
Only common tests should be described solely by name; describe more complex techniques in the Methods section.
- A description of all covariates tested
- A description of any assumptions or corrections, such as tests of normality and adjustment for multiple comparisons
- A full description of the statistical parameters including central tendency (e.g. means) or other basic estimates (e.g. regression coefficient) AND variation (e.g. standard deviation) or associated estimates of uncertainty (e.g. confidence intervals)
- For null hypothesis testing, the test statistic (e.g. F , t , r) with confidence intervals, effect sizes, degrees of freedom and P value noted
Give P values as exact values whenever suitable.
- For Bayesian analysis, information on the choice of priors and Markov chain Monte Carlo settings
- For hierarchical and complex designs, identification of the appropriate level for tests and full reporting of outcomes
- Estimates of effect sizes (e.g. Cohen's d , Pearson's r), indicating how they were calculated

Our web collection on [statistics for biologists](#) contains articles on many of the points above.

Software and code

Policy information about [availability of computer code](#)

Data collection

Flow cytometric analyses were performed with BD FACSVerser , Violet(2), Blue(4), Red(2)
Quantitative PCR was performed with Applied Biosystems QuantStudio™ 3 Real-Time PCR System

Data analysis

Flow cytometric data was analysed with FlowJo v10.7.1
Consensus sequences for viral genome sequencing were generated using Medaka v1.5.0. Protein homology model was generated using YASARA v21.8.26. Calculations on mutations were performed in Bioluminate (Schrodinger Release 2020-4). Figures were generated in PyMOL v2.5. Software used was installed and configured by SBGrid v7.0.
All other data was analysed and graphed with GraphPad Prism 8 v8.4.2 and Microsoft Excel v16.56

For manuscripts utilizing custom algorithms or software that are central to the research but not yet described in published literature, software must be made available to editors and reviewers. We strongly encourage code deposition in a community repository (e.g. GitHub). See the Nature Research [guidelines for submitting code & software](#) for further information.

Data

Policy information about [availability of data](#)

All manuscripts must include a [data availability statement](#). This statement should provide the following information, where applicable:

- Accession codes, unique identifiers, or web links for publicly available datasets
- A list of figures that have associated raw data
- A description of any restrictions on data availability

The data supporting the findings of this study are documented within the paper and are available from the corresponding authors upon request. Correspondence and requests for materials should be addressed to: Stanley Perlman (stanley-perlman@uiowa.edu) or Paul B. McCray, Jr. (paul-mccray@uiowa.edu). Source data

obtained from all experiments involved in the manuscript has been uploaded. Human datasets were obtained from GEO accession GSE150910 and GTEX portal (<https://www.gtexportal.org/home/>) for analysis. Sequence of mouse-adapted virus was deposited in GISAID (Accession ID: EPI_ISL_1666328).

Field-specific reporting

Please select the one below that is the best fit for your research. If you are not sure, read the appropriate sections before making your selection.

Life sciences Behavioural & social sciences Ecological, evolutionary & environmental sciences

For a reference copy of the document with all sections, see [nature.com/documents/nr-reporting-summary-flat.pdf](https://www.nature.com/documents/nr-reporting-summary-flat.pdf)

Life sciences study design

All studies must disclose on these points even when the disclosure is negative.

Sample size	Numbers of mice analyzed were based on previous studies and on the numbers required to obtain statistical significance (e.g. Zheng et al, Nature 589:603-607, 2021) PMID: 33166988, No sample size calculation was performed in advance.
Data exclusions	No data were excluded
Replication	All experiments were repeated at least twice with the same results. The number (n) of biological replicates or animals is indicated as an exact number in the figure legends.
Randomization	Mice were randomly assigned to each group in each experiment.
Blinding	Since all of the studies were performed in the BSL3 laboratory, blinding was not possible because of biosafety considerations. All histopathological scoring was performed in a blinded manner, by a board-certified pathologist.

Reporting for specific materials, systems and methods

We require information from authors about some types of materials, experimental systems and methods used in many studies. Here, indicate whether each material, system or method listed is relevant to your study. If you are not sure if a list item applies to your research, read the appropriate section before selecting a response.

Materials & experimental systems

n/a	Involved in the study
<input type="checkbox"/>	<input checked="" type="checkbox"/> Antibodies
<input type="checkbox"/>	<input checked="" type="checkbox"/> Eukaryotic cell lines
<input checked="" type="checkbox"/>	<input type="checkbox"/> Palaeontology and archaeology
<input type="checkbox"/>	<input checked="" type="checkbox"/> Animals and other organisms
<input type="checkbox"/>	<input checked="" type="checkbox"/> Human research participants
<input checked="" type="checkbox"/>	<input type="checkbox"/> Clinical data
<input checked="" type="checkbox"/>	<input type="checkbox"/> Dual use research of concern

Methods

n/a	Involved in the study
<input checked="" type="checkbox"/>	<input type="checkbox"/> ChIP-seq
<input type="checkbox"/>	<input checked="" type="checkbox"/> Flow cytometry
<input checked="" type="checkbox"/>	<input type="checkbox"/> MRI-based neuroimaging

Antibodies

Antibodies used	Live/Dead Fixable Aqua Dead Cell Satin Kit (ThermoScientific, Cat. No.: L34957); APC α -mouse CD220 (clone RA3-6B2, Cat. No.: 553092); APC/Cyanine 7 α -mouse CD3e (clone 145-2C11, Cat. No.: 100330); APC/Cyanine 7 α -mouse CD11c (clone HL3; Cat. No.: 561241); FITC α -mouse Ly6G (clone 1A8; Cat. No.: 127606); PE α -mouse CD11b (clone M1/70; Cat. No.: 101208); eFluor450 α -mouse CD11b (clone M1/70; Cat. No.: 48011282); PE/Cyanine 7 α -mouse CD8 (clone 53-6.7; Cat. No.: 100722); PerCP/Cyanine 5.5 α -mouse CD4 (clone RM4.5; Cat. No.: 550954); PerCP/Cyanine 5.5 α -mouse Ly6C (clone HK1.4; Cat. No.: 128012); PE α -mouse Siglec F (clone E50-2440; Cat. No.: 562068); PE-Cy7 α -mouse CD45 (clone 30-F11; Cat. No.: 103113); Rabbit monoclonal antibody against SARS-CoV-2 N protein (Cat. No.: 40143-R019) PE α -mouse CD 64 (clone X54-5/7.1; Cat. No.: 139304)
Validation	All antibodies were obtained commercially and validated for flow cytometric analysis in mice by the manufacturers. Specificity and sensitivity were validated by the manufacturers.

Eukaryotic cell lines

Policy information about [cell lines](#)

Cell line source(s)	Calu-3 and Vero E6 cells (ATCC)
Authentication	None of the cells were formally authenticated although they remained sensitive to infection with SARS-CoV-2.
Mycoplasma contamination	Negative for Mycoplasma
Commonly misidentified lines (See ICLAC register)	No commonly misidentified cell lines were used.

Animals and other organisms

Policy information about [studies involving animals](#); [ARRIVE guidelines](#) recommended for reporting animal research

Laboratory animals	Male and female C57BL/6 and BALB/c mice; 6-10 week old for young mice; 6 month old for aged mice.
Wild animals	None
Field-collected samples	None
Ethics oversight	All animal studies were approved by the University of Iowa Animal Care and Use Committee and meet stipulations of the Guide for the Care and Use of Laboratory Animals.

Note that full information on the approval of the study protocol must also be provided in the manuscript.

Human research participants

Policy information about [studies involving human research participants](#)

Population characteristics	<i>Describe the covariate-relevant population characteristics of the human research participants (e.g. age, gender, genotypic information, past and current diagnosis and treatment categories). If you filled out the behavioural & social sciences study design questions and have nothing to add here, write "See above."</i>
Recruitment	<i>Describe how participants were recruited. Outline any potential self-selection bias or other biases that may be present and how these are likely to impact results.</i>
Ethics oversight	<i>Identify the organization(s) that approved the study protocol.</i>

Note that full information on the approval of the study protocol must also be provided in the manuscript.

Flow Cytometry

Plots

Confirm that:

- The axis labels state the marker and fluorochrome used (e.g. CD4-FITC).
- The axis scales are clearly visible. Include numbers along axes only for bottom left plot of group (a 'group' is an analysis of identical markers).
- All plots are contour plots with outliers or pseudocolor plots.
- A numerical value for number of cells or percentage (with statistics) is provided.

Methodology

Sample preparation	Mice were anesthetized with ketamine/xylazine before dissecting for lung harvest. Lungs were perfused transcatheterially and minced into smaller pieces with a pair of surgical scissors. The minced lungs were left in digestion buffer (1 mg/ml collagenase D (Roche) and 0.1 mg/ml DNase I (Roche)) at 37°C for 30 minutes. Digested tissue was passed through a 70 µm cell strainer and cells were pelleted by centrifugation at 330 RCF for 5 minutes. Blood was collected by retro orbital bleeding in collection tube coated with anti-coagulant. Collected blood was transferred to ACK buffer and then washed in excess PBS. Cell pellet was resuspended in either FACS buffer or RPMI for peptide stimulation. Fc receptor on cells were block and subsequently fixed with Cytofix/cytoperm followed by intracellular IFN γ and TNF staining after peptide stimulation. Cells were pelleted and resuspended in FACS buffer for analysis.
Instrument	BD FACSVerser , Violet(2), Blue(4), Red(2)
Software	FlowJo v10.7.1
Cell population abundance	Virus-specific CD4+ T cells frequency from lungs range from 0.33 to 2.49%

Cell population abundance

Virus-specific CD8+ T cells frequency from lungs range from 0.3 to 2.57%
 B cell frequency from lungs range from 1.56 to 16.6%
 IMMs frequency from lungs range from 4.31 to 17.8%
 PMN frequency from lungs range from 0.087 to 4.81%
 AM frequency from lungs range from 0.0071 to 0.27%
 Eosinophils frequency from lungs range from 0.23 to 0.83%
 CD45+ frequency in the blood range from 24.6 to 92.7 %
 PMN frequency in the blood range from 10.59 to 47.84%
 B cell frequency in the blood range from 8.81 to 26.76%
 Total T cells frequency in the blood range from 2.39 to 23.96%
 CD4+ T cells frequency in the blood range from 1.18 to 12.44%
 CD8+ T cells frequency in the blood range from 0.99 to 47.84%

Gating strategy

Lymphocytes were gated on SSC-A vs FSC-A. Single cells were gated on lymphocyte gate using FSC-W/H vs FSC-A. Live cells were gated on single cell gate with FSC-A/H vs Live/Dead. CD45+ cells were gated on FSC-A /H vs CD45. B and T cells were gated on B220 vs CD3 as B220+ and CD3+ population respectively from the CD45+ cell population. CD8+ and CD4+ T cells were gated on CD3+ population on CD8 vs CD4. PMN were gated on Ly6G vs CD11b on CD45+ cell population as Ly6G+ CD11b+ population. AMs and eosinophils were gated on Siglec F vs CD11b as CD11b- Siglec F+ and CD11b+ Siglec F+ population respectively from Ly6G- population of the previous gate (Ly6G vs CD11b). IMMs were gated on Ly6C vs CD11b as CD11b+ Ly6C+ population from the Siglec F- population of the previous gate (Siglec F vs CD11b).

Tick this box to confirm that a figure exemplifying the gating strategy is provided in the Supplementary Information.